DES 2016-0175
FERMILAB-PUB-17-043

DES Science Portal: I - Computing Photometric Redshifts

Julia Gschwend[a,b,*], Aurelio Carnero[a,b], Ricardo L.C. Ogando[a,b], Angelo F. Neto[b,c], Marcio A.G. Maia[a,b], Luiz A.N. da Costa[a,b], Marcos Lima[d,b], Paulo S. Pellegrini[a,b], Riccardo Campisano[b,e], Cristiano P. Singulani[a,b], Carlos A. Souza[b], Matias Carrasco Kind[f], Tamara M. Davis[g,h], Juan De Vicente[i], Will Hartley[j], Ben Hoyle[k], Antonella Palmese[l], Markus Rau[k,m], Iftach Sadeh[n], Filipe B. Abdalla[l,o], Sahar Allam[p], Jacobo Asorey[g,h], Aurelién Benoit-Lévy[l,q], Emmanuel Bertin[q], David Brooks[l], Elizabeth Buckley-Geer[p], Jorge Carretero[r], Francisco J. Castander[s], Carlos Cunha[t], Chris D'Andrea[u], Darren DePoy[v], Shantanu Desai[w], Peter Doel[l], Tim Eifler[x,y], August Evrard[z,aa], Pablo Fosalba[s], Josh Frieman[p,ab], Juan García-Bellido[ac], Enrique Gaztanaga[s], Tommaso Giannantonio[ad,ae], Karl Glazebrook[h], Robert Gruendl[af,ag], Gaston Gutierrez[p], Samuel Hinton[g,h], Janie Hoormann[g], David James[ah,ai], Anthea King[aj,h], Kyler Kuehn[ak], Nikolay Kuropatkin[p], Ofer Lahav[l], Geraint Lewis[al], Chris Lidman[ak], Edward Macaulay[am], Marisa March[u], Jennifer Marshall[v], Paul Martini[an,ao], Felipe Menanteau[af,ag], Ramon Miquel[ap,r], Anais Möller[aq,h], Dale Mudd[ao], Andrés Plazas[y], Kathy Romer[ar], Eusebio Sanchez[i], Basilio Santiago[as,b], Vic Scarpine[p], Ignacio Sevilla-Noarbe[i], Robert Sharp[aq], Mathew Smith[at], Marcelle Soares-Santos[p], Flavia Sobreira[au,b], Natalia Eiré Sommer[av,h], Eric Suchyta[aw], Molly Swanson[ag], Brad E. Tucker[h,aq], Douglas Tucker[p], Syed Uddin[ax,h], Alistair Walker[ai], Bonnie R. Zhang[aq,h]

[a] *Observatório Nacional, Rua General José Cristino, 77, Rio de Janeiro, RJ, 20921-400, Brazil*
[b] *Laboratório Interinstitucional de e-Astronomia - LIneA, Rua General José Cristino, 77, Rio de Janeiro, RJ, 20921-400, Brazil*
[c] *LSST Project Management Office, Tucson, AZ, USA*
[d] *Departamento de Física Matemática, Instituto de Física, Universidade de São Paulo, CP 66318, São Paulo, SP, 05314-970, Brazil*
[e] *Centro Federal de Educação Tecnológica Celso Suckow da Fonseca - CEFET/RJ, Av. Maracanã, 229, Rio de Janeiro, RJ, 20271-110, Brazil*
[f] *Department of Astronomy, University of Illinois, MC-221, 1002 W. Green Street, Urbana, IL 61801, US*
[g] *School of Mathematics and Physics, University of Queensland, QLD 4072, Australia*
[h] *ARC Centre of Excellence for All-sky Astrophysics (CAASTRO), Australia*
[i] *Centro de Investigaciones Energéticas, Medioambientales y Tecnológicas (CIEMAT), Avda. Complutense 40, E-28040, Madrid, Spain*
[j] *Department of Physics, ETH Zurich, Wolfgang-PauliStrasse 16, CH-8093 Zurich, Switzerland*
[k] *Universitäts-Sternwarte, Fakultät für Physik, Ludwig-Maximilians Universität München, Scheinerstr. 1, D-81679 München, Germany*
[l] *Department of Physics & Astronomy, University College London, Gower Street, London, WC1E 6BT, UK*
[m] *Max-Planck-Institut für extraterrestrische Physik, Giessenbachstrasse 1, 85748 Garching, Germany*
[n] *DESY-Zeuthen, D-15738 Zeuthen, Germany*
[o] *Department of Physics and Electronics, Rhodes University, PO Box 94, Grahamstown, 6140, South Africa*
[p] *Fermi National Accelerator Laboratory, P. O. Box 500, Batavia, IL 60510, USA*
[q] *Sorbonne Universités, UPMC Univ Paris 06, UMR 7095, Institut d'Astrophysique de Paris, F-75014, Paris, France*
[r] *Institut de Física d'Altes Energies (IFAE), The Barcelona Institute of Science and Technology, Campus UAB, 08193 Bellaterra (Barcelona) Spain*
[s] *Institut de Ciències de l'Espai, IEEC-CSIC, Campus UAB, Carrer de Can Magrans, s/n, 08193 Bellaterra, Barcelona, Spain*
[t] *Kavli Institute for Particle Astrophysics & Cosmology, P.O. Box 2450, Stanford University, Stanford, CA 94305, USA*
[u] *Department of Physics and Astronomy, University of Pennsylvania, Philadelphia, PA 19104, USA*
[v] *George P. and Cynthia Woods Mitchell Institute for Fundamental Physics and Astronomy, and Department of Physics and Astronomy, Texas A&M University, College Station, TX 77843, USA*
[w] *Department of Physics, IIT Hyderabad, Kandi, Telangana 502285, India*
[x] *Department of Physics, California Institute of Technology, Pasadena, CA 91125, USA*
[y] *Jet Propulsion Laboratory, California Institute of Technology, 4800 Oak Grove Dr., Pasadena, CA 91109, USA*
[z] *Department of Astronomy, University of Michigan, Ann Arbor, MI 48109, USA*
[aa] *Department of Physics, University of Michigan, Ann Arbor, MI 48109, USA*
[ab] *Kavli Institute for Cosmological Physics, University of Chicago, Chicago, IL 60637, USA*
[ac] *Instituto de Fisica Teorica UAM/CSIC, Universidad Autonoma de Madrid, 28049 Madrid, Spain*
[ad] *Institute of Astronomy, University of Cambridge, Madingley Road, Cambridge CB3 0HA, UK*
[ae] *Kavli Institute for Cosmology, University of Cambridge, Madingley Road, Cambridge CB3 0HA, UK*
[af] *Department of Astronomy, University of Illinois, 1002 W. Green Street, Urbana, IL 61801, USA*
[ag] *National Center for Supercomputing Applications, 1205 West Clark St., Urbana, IL 61801, USA*
[ah] *Astronomy Department, University of Washington, Box 351580, Seattle, WA 98195, USA*
[ai] *Cerro Tololo Inter-American Observatory, National Optical Astronomy Observatory, Casilla 603, La Serena, Chile*
[aj] *School of Physics, University of Melbourne, Parkville, VIC 3010, Australia*
[ak] *Australian Astronomical Observatory, North Ryde, NSW 2113, Australia*
[al] *Sydney Institute for Astronomy, School of Physics, A28, The University of Sydney, NSW 2006, Australia*
[am] *Institute of Cosmology & Gravitation, University of Portsmouth, Portsmouth, PO1 3FX, UK*
[an] *Center for Cosmology and Astro-Particle Physics, The Ohio State University, Columbus, OH 43210, USA*
[ao] *Department of Astronomy, The Ohio State University, Columbus, OH 43210, USA*
[ap] *Institució Catalana de Recerca i Estudis Avançats, E-08010 Barcelona, Spain*
[aq] *Research School of Astronomy and Astrophysics, Australian National University, Canberra, ACT 2611, Australia*
[ar] *Department of Physics and Astronomy, Pevensey Building, University of Sussex, Brighton, BN1 9QH, UK*
[as] *Instituto de Física, UFRGS, Caixa Postal 15051, Porto Alegre, RS - 91501-970, Brazil*
[at] *School of Physics and Astronomy, University of Southampton, Southampton, SO17 1BJ, UK*
[au] *Instituto de Física Gleb Wataghin, Universidade Estadual de Campinas, Campinas, SP, 13083-859, Brazil*
[av] *Mount Stromlo Observatory, Research School of Astronomy and Astrophysics, Australian National University, Canberra, ACT 2611, Australia*
[aw] *Computer Science and Mathematics Division, Oak Ridge National Laboratory, Oak Ridge, TN 37831, USA*
[ax] *Purple Mountain Observatory, Chinese Academy of Sciences, Nanjing, Jiangsu, China*

Abstract

We present the Dark Energy Survey (DES) Science Portal, an integrated web-based data interface designed to facilitate scientific analysis. We demonstrate how the Portal can provide a reliable environment to access complete data sets, provide validation algorithms and metrics in the case of multiple methods and training configurations, and maintain the provenance between the different steps of a complex calculation, while ensuring reproducibility of the results. We use the estimation of DES photometric redshifts (photo-zs) as an example. A significant challenge facing photometric surveys for cosmological purposes, such as DES, is the need to produce reliable redshift estimates. The choice between competing algorithms and configurations and the maintenance of an up-to-date spectroscopic database to build training sets, for example, are complex tasks when dealing with large amounts of data that are regularly updated and constantly growing. We show how the DES Science Portal can be used to train and validate several photo-z algorithms using the DES first year (Y1A1) data. The photo-zs estimated in the Portal are used to feed the creation of catalogs for scientific workflows. While the DES collaboration is still developing techniques to obtain precise photo-zs, having a structured framework like the one presented here is critical for the systematic vetting of DES algorithmic improvements and the consistent production of photo-zs in future DES releases.

Keywords

astronomical databases: catalogs, surveys – methods: data analysis – galaxies: distances and redshifts, statistics

1. Introduction

In the last few decades, galaxy surveys have become one of the main research tools in astronomy, in particular, for the study of cosmology. The need for increasing statistical samples and depths have encouraged the design and construction of bigger and wider surveys around the world. These projects are generating vast amounts of data, which have made astronomy enter the realm of big data, making more challenging the cosmological analysis.

In this context, the Dark Energy Survey (DES, Flaugher, 2005; DES et al., 2016) collaboration proposed, along with the Data Management system (DESDM[1], Mohr et al., 2012, - see Section 2.1 for details), the creation of a dedicated portal to solve some of the problems associated with the data processing, the so-called DES Science Portal. In the future, the Portal will interconnect the Data Release database with the coadded images for exploration and visualization of the data. Moreover, one form of public access to DES data will be with the help of this infrastructure, into an online interface.

In this paper, we present the capabilities of the DES Science Portal to produce photometric redshifts (photo-zs) for the DES collaboration. The DES Science Portal provides an integrated environment where all the steps necessary to compute photo-zs can be carried out in a controlled and consistent way. It produces galaxy samples with photo-zs in the form of pruned lightweight catalogs containing only the columns required by specified science analysis workflows, which are also integrated into the Portal (Fausti et al. 2017, in preparation).

The automatic provenance, configuration management, and the computing facilities that sustain the portal allow for a sampling of many photo-z settings, which would be highly time-consuming without an infrastructure such as this. The need for the Portal capabilities will increase as the DES databases grow, and more generally, as we enter an era of Big Data astronomy.

The DES is a 5-year program to carry out two distinct surveys. The wide-angle survey covers 5,000 deg^2 of the southern sky in five ($grizY$) filters to a nominal magnitude limit of $\sim$24 in most bands. Also, there is a deep survey (i $\sim$26) of about 30 deg^2 in four filters ($griz$) with a well-defined cadence to search for type-Ia Supernovae (SNe Ia) (Kessler et al., 2015). The primary goal of the DES is to constrain the nature of dark energy through the combination of four observational probes, namely baryon acoustic oscillations, counts of galaxy clusters, weak gravitational lensing, and determination of distances of SNe.

The constraining power of DES cosmological results will strongly depend on the ability to estimate reliable photometric redshifts (photo-z, e.g., Huterer et al., 2004; Ma et al., 2006; Lima and Hu, 2007; Ma and Bernstein, 2008; Hearin et al., 2010; Cunha et al., 2014; Georgakakis et al., 2014). In fact, the computation of accurate photo-zs has been one of the major concerns of the collaboration, which has spurred the implementation and testing of several algorithms. For instance, Sánchez et al. (2014) addressed the performance of several codes when applied to the DES science verification data (SVA1), while Banerji et al. (2015) discussed the impact of using infrared data. More recently, Bonnett et al. (2016) examined the impact of four photo-z algorithms on the conclusions of the first DES cosmological analysis based on weak lensing discussed by Abbott et al. (2016).

Photo-z estimation will only get more challenging for future DES releases and future photometric surveys. The reason is that we are sampling magnitudes beyond the reach of most spectroscopic surveys and therefore, traditional photo-z validations are not realistic. This has inspired the implementation of new ideas in the collaboration, such as the calibration of photo-zs with cross-correlations (Newman, 2008), the training and validation of photo-z codes with simulations (data-augmentation) (Hoyle et al., 2015) and validation of photo-zs with spectrophotometric samples like the Cosmic Evolution Survey (COSMOS, Scoville et al., 2007) and the Advanced Large Homogeneous Area Medium Band Redshift Astronomical Survey (ALHAMBRA, Moles et al., 2008). These techniques are under development within the collaboration on a parallel track with the elaboration of the Portal tools. Therefore, the photo-z methods and catalogs described here are not necessarily the ones used in DES cosmological analyses. Techniques for assignment and validation of

*Corresponding author

Email address: julia@linea.gov.br (Julia Gschwend)

[1] http://www.darkenergysurvey.org/the-des-project/survey-and-operations/data-management/

photo-zs for DES are under continuous development and will be implemented in the Science Portal as they become ready for use.

As an example of usage of the Portal, we show a sequence of tasks that include the preparation of a spectroscopic sample by combining data from different redshift surveys, the creation of training sets, the training and validation procedures for several algorithms, and the computation of photo-zs for large datasets. To show these examples, we used the DES first year data release, referred as Y1A1 (Y1A1 data release paper, in preparation). The algorithms used in this demonstration are: ANNZ (Collister and Lahav, 2004), ANNZ2 (Sadeh et al., 2016), ARBORZ (Gerdes et al., 2010), DNF (De Vicente et al., 2016), LEPHARE (Arnouts et al., 2002; Ilbert et al., 2006), POFZ (Cunha et al., 2009), SKYNET (Graff et al., 2014), and TPZ (Carrasco Kind and Brunner, 2013, 2014). More elaborate schemes are being implemented in the Portal and can be used for future analyses, e.g., the usage of probability density functions (PDFs) instead of point estimates.

The outline of this paper is as follows. In Section 2, we present the data used. In Section 3, we describe the procedures and pipelines available in the Portal to compute photometric redshifts and to carry out tests that evaluate their quality. In Section 4 we present a few examples of how the Science Portal can aid to determine reliable photo-zs. Finally our conclusions are presented in Section 5.

Also, we present, attached to this text, a list[2] of five videos (V0 to V4), showing examples of live runs, in a guided tour through the photo-z pipelines.

2. The Data

2.1. Photometric data

The DES observations are carried out with the mosaic camera DECam (Flaugher et al., 2015; Honscheid et al., 2014), built as part of DES project and mounted on the 4-meter Blanco telescope at the Cerro Tololo Inter-American Observatory (CTIO), in Chile. The data are reduced and calibrated by the DES Data Management (DESDM) team at the National Center for Supercomputing Applications (NCSA) using standard procedures described by Desai et al. (2012), Mohr et al. (2012), and Gruendl et al. 2017 (in preparation). This system is used for the processing and calibration of DES data, and the DECam Community Pipeline. The observations (Diehl et al., 2014) reported here took place from August 2013 to February 2014 and include a total of 14,340 exposures in the *grizY* filters, covering a total area of ∼1,800 deg^2 in eight distinct regions, making the so-called DES Y1 release.

The two largest regions are part of the wide-field survey. One of about 160 deg^2 overlapping the Sloan Digital Sky Survey Stripe 82 Imaging Data (S82, Jiang et al., 2014), and another of ∼1,600 deg^2 overlapping the region observed by the South Pole Telescope (SPT, Carlstrom et al., 2011). These two wide regions were covered with up to four passes in each filter, reaching a SExtractor's `mag_auto` magnitude limit of i ∼22.5 in the AB system for a 10σ detection limit.. In this work, we only used S82 as an example of a wide field. The remaining regions, called "supplemental fields" — where a large number of spectroscopic redshifts (spec-zs) are available — belong to both the science verification phase[3] (SVA1), and of the Y1 release. Four of these regions are collectively known as Supernova (SN) fields. One of the other regions overlaps with the VVDS-14h field from VIMOS VLT Deep Survey (hereafter VVDS, Le Fèvre et al., 2005) and the final region overlaps with COSMOS. The SN fields are regularly observed as part of the SNe Ia program, making available a greater number of exposures compared to the wide survey. The locations of these regions are shown in Figure 1 along with the DES footprint.

We use the SOURCE EXTRACTOR (SExtractor, Bertin and Arnouts, 1996; Bertin, 2011) catalogs produced from these co-added images. In our case, we arbitrarily use SExtractor's `mag_detmodel` magnitudes as input data in the tests shown in Section 4, although there are several other magnitude types available. We eliminate objects outside the physical color range -2.0 to 4.0 for g-r, r-i and i-z and consider only objects with `Flag=0` (clean detection). These settings are similar to those utilized in the analysis of the science verification data (e.g., Sánchez et al., 2014; Bonnett et al., 2016; Giannantonio et al., 2016; Melchior et al., 2016).

In Figure 2 we show the i-band and color g-r distributions for all the fields considered (grouping the SN fields in a single set). The main properties of the datasets are presented in Table 1. Note that each supplemental field composes two distinct datasets referred to as D04 and DFULL. The first corresponds to the catalogs extracted from the co-addition of four single epoch exposures, aiming to reproduce the mean depth obtained in the Y1 wide fields SPT and S82. On the other hand, DFULL corresponds to the catalogs extracted from the combination of all the available single epoch exposures in the field. Except for the VVDS field, the DFULL datasets are deeper than D04 and those of the wide-field survey. Note that the exposures used to make the D04 and DFULL sets also had to meet the quality cuts defined for the DES wide-field survey. In general, these fields were observed with different observing conditions, and therefore it was difficult to mimic the wide survey for Y1 in the supplemental fields. In subsequent years an effort has been made to amend that situation. The vertical dashed lines in Figure 2 refer to the approximate magnitude limits in these datasets, defined as the magnitude corresponding to the maximum of the distribution. These values are calculated before any pruning in the samples. The photometric sample was also corrected for extinction using the corrections delivered by DESDM, which are inferred from the extinction maps by Schlegel et al. (1998).

2.2. Spectroscopic data

In this paper, we use a spectroscopic redshift sample with reliable measurements to train photo-z algorithms, and to test

[2] `https://www.youtube.com/playlist?list=PLGFEWqwqBauBIYa8H6KnZ4d-5ytM59vG2`

[3] `https://des.ncsa.illinois.edu/releases/sva1`

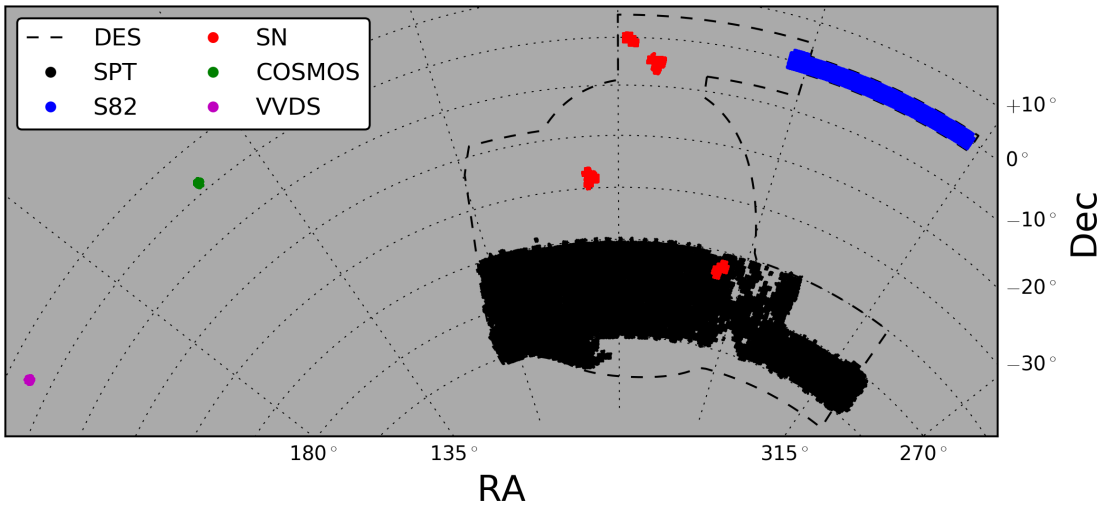

Figure 1: Location of all the Y1A1 fields used in this paper and DES footprint (dashed line).

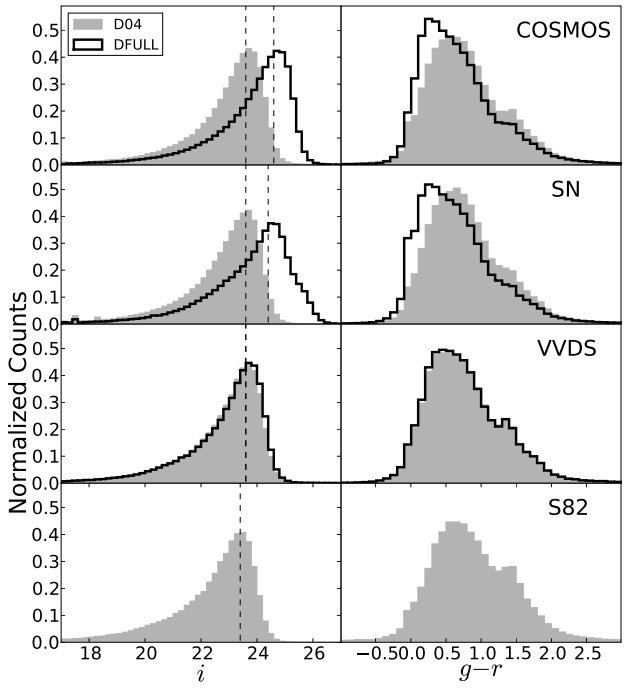

Figure 2: Magnitude (i-band) and color (g-r) distributions for all the fields used in this paper. The dashed lines refer to the peak of magnitude distributions, with values presented in Table 1. The DFULL sample (see text) includes all the exposures taken at the time of the Y1A1 release.

Table 1: DES fields considered in this paper.

Field	Dataset	Objects	Matches$^{\diamond}$	Area†	Mag lim‡
COSMOS	D04	313,380	3,483	2.97	23.6
	DFULL	599,139	3,544	3.04	24.6
SN	D04	2,569,018	34,683	31.76	24.4
	DFULL	4,761,997	26,477	31.73	24.6
VVDS	D04	260,446	2,473	2.91	23.6
	DFULL	271,518	2,461	2.91	23.6
S82	–	12,487,566	42,158	165.84	23.4

$\diamond$ Spectroscopic matches: see Section 3.2.
† Approximate area covered in deg^2.
‡ Magnitude limit in i-band (the peak of number counts)

their performance, as an example of validation procedure. This sample is constructed by compiling data available from a large number of surveys that were individually ingested into the database associated to DES Science Portal.

Currently, in the Portal database, there are redshift measurements from a total of 31 galaxy spectroscopic surveys available in the literature. In total, these catalogs contain 1,053,343 objects, where ~93% are extragalactic sources including both galaxies and quasars. We selected galaxies with high-quality spec-z, reducing the sample to 841,057 measurements. Some of these measurements are different observations of the same object, i.e., they have been observed in more than one survey. After dealing with multiple measurements in the spectroscopic database (see discussion of how this is done in Section 3), we end up with 759,890 unique high quality spec-zs.

We note that the data are dominated by low redshift surveys (see Figure 3). However, we know that not all of these sources will be matched to the photometric sample since they extend beyond the Y1A1 DES footprint. Therefore, the number of spectroscopic redshifts matched to DES photometry will be smaller than the number of spec-zs in our database (see Sec-

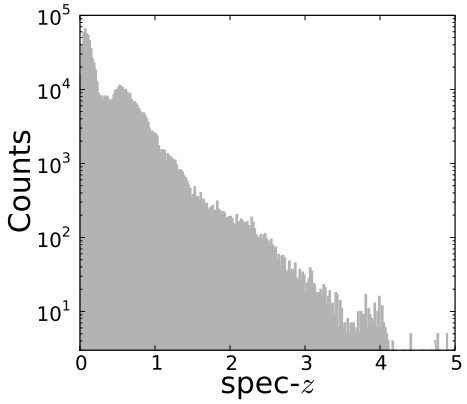

Figure 3: Spectroscopic redshift distribution of all galaxies in the spectroscopic database, after resolving duplicates and after selecting the ones with high quality spec-zs.

tion 3). In particular, around 250,000 sources overlap with Y1 footprint.

In Table 2 we show the information about all spectroscopic surveys present in the spectroscopic database at the time of writing, ordered by the number of successful matches with the Y1A1 data (S82, COSMOS D04, SN D04 and VVDS14 D04 datasets). Those numbers includes all matches for each survey, so the total number in the table includes objects with multiple measurements due to the overlap in area covered by the surveys.

3. Methodology

As mentioned earlier all the results presented in this paper were produced using the DES Science Portal. The Portal has been conceived as an overarching web-based system integrated with two databases: one for administration and other one to store the data.

The structural organization of the DES Science Portal is presented schematically in Figure 4. The Portal consists of four different stages: Data Installation, Data Preparation, Catalog Creation, and Science Pipelines. Each stage groups a list of pipelines in Extensible Markup Language, which concatenate components (Python wrappers calling algorithms of different languages). The chaining of tasks needed to create catalogs called "end-to-end" (E2E), is delineated by the gray dashed area. The group of pipelines related to the photo-z calculation, highlighted in blue, is fed with DES co-added photometric catalog, as well as a spectroscopic catalog.

The DES Science Portal allows for quick changes in configurations and input data, automatically produces figures and tables with validation metrics, facilitating comparisons and expediting performance improvements. The Portal registers the history of versions of pipelines, components, and algorithms. It enables the access to code versions, thus allowing complete reproducibility of the results.

A full description of the Portal is beyond the scope of the present paper, and here we only describe the second stage which deals with the steps required for the calculation photo-zs, highlighted in Figure 5. The pipelines *Spectroscopic Sample*, *Training Set Maker*, *Photo-z Training*, and *Photo-z Compute* are represented in green, while both the input data and output products are represented in yellow. The first two pipelines are used to prepare the training and validation sets that will be employed for the photo-z algorithms. The last two are responsible for performing the training (and validation) and computing the photo-zs for the photometric data, respectively. The video V0[4] is an overview of the Portal structure, especially covering the pipelines related to the photo-z calculation.

Details about the usage of the four photo-z pipelines are presented in the videos V1 to V4 (see below). Here, we show one example of the Portal interface in Figure 6, using one of the first pipelines in the photo-z cycle, the creation of the *Spectroscopic Sample*. The interface is organized into three steps, corresponding to the tabs in the pipeline top menu. This structure is present in all pipelines in the Portal. These are:

- Choice of *Input Data*, where the user selects the input data, in this case, the spectroscopic surveys of interest, from the 31 presently available (listed in Table 2).
- Choice of *Configuration* of each component. The list of components that belong to the pipeline concerned (in this case, there is only one) is displayed on the left menu. There, the user can select among the components the specific configuration for each one. Below that, there is a set of buttons from the configuration manager, a tool that allows the user to save the most frequently used configurations, which is useful for repeated tests. In our example, we can choose the quality threshold of the spec-zs, the spectral type and the criteria used to resolve multiple measurements.
- In the *Summary*, the Portal displays a list of the decisions taken in the previous steps so that the user can check and confirm, just before the job submission. Finally, a brief comment is required, to characterize the purpose of this run.

We use the case of the Y1A1 data release to illustrate the capabilities and the benefits offered by the Portal. However, the examples presented here are not the basis of upcoming Y1A1 cosmology papers. They are arbitrary examples of applications, where we take the opportunity to investigate some particular issues related to the production of value-added quantities to built astronomical catalogs, in particular, those related to the photo-z calculation. These include handling of the data, built-in parallelization of the processes whenever beneficial, and a complete record of each executed actions and process, thus enabling the user to track how any product was created and reproduce the results. The benefits of the Science Portal become most relevant as the dataset grows in size and complexity. The calculation of photo-zs is a good illustration of that.

[4] https://youtu.be/9zy0vXAWUdU?list=PLGFEWqwqBauBIYa8H6KnZ4d-5ytM59vG2

Table 2: Spectroscopic samples used in this paper.

Survey	# of matches	%	z mean	z min	z max	Ref. ‡
2DF	218,932	28.8	0.12	0.00	3.50	1
6DF	107,266	14.1	0.07	0.00	3.79	2
DR7	89,282	11.7	0.17	0.00	4.21	3
WIGGLEZ	80,875	10.6	0.59	0.00	6.09	4
DR12 CMASS	51,381	6.8	0.57	0.00	7.01	5
DEEP2	35,205	4.6	0.87	0.01	3.43	6
LCRS	23,268	3.1	0.11	0.00	0.32	7
DR12 LOWZ	21,383	2.8	0.30	0.01	6.11	5
EBOSS DES ELG	20,547	2.7	0.91	0.00	7.01	8
3DHST	20,339	2.7	1.10	0.01	4.00	9
VIPERS	14,757	1.9	0.68	0.04	4.40	10
VVDS	14,714	1.9	0.61	0.00	4.54	11
DES AAOMEGA	14,381	1.9	0.61	0.00	4.77	12
ZCOSMOS	12,630	1.7	0.54	0.00	1.99	13
SDSS	8,708	1.1	0.54	0.00	5.66	14
GAMA	7,656	1.0	0.22	0.01	0.74	15
ACES	4,338	0.6	0.59	0.01	2.84	16
ATT archive	3,458	0.5	0.22	0.00	3.38	17
XXL AAOMEGA	3,143	0.4	0.91	0.00	4.66	18
PANSTARRS	1,792	0.2	0.80	0.00	4.31	19
UDS	1,411	0.2	1.12	0.00	4.79	20
SNLS FORS	1,353	0.2	0.54	0.01	3.76	21
ATLAS	753	0.1	0.39	0.00	3.20	22
SPARCS	403	0.1	0.92	0.12	1.76	23
CDB	392	0.1	0.63	0.08	2.54	24
GLASS	383	0.1	1.16	0.20	2.54	25
SNLS AAOmega	358	<0.1	0.63	0.03	2.10	26
FMOS COSMOS	328	<0.1	1.56	0.75	2.49	27
VUDS	245	<0.1	2.26	0.10	4.91	28
MOSFIRE	113	<0.1	2.31	0.80	3.71	29
STALIN	96	<0.1	1.15	0.04	3.87	30

‡ References: 1- Colless et al. (2001) `http://www.2dfgrs.net/`; 2- Jones et al. (2009) and `http://www.6dfgs.net/`; 3- Abazajian et al. (2009) and `http://classic.sdss.org/dr7/`; 4- Parkinson et al. (2012) and `http://wigglez.swin.edu.au/site/`; 5- Alam et al. (2015) and `http://www.sdss.org/dr12/`; 6- Davis et al. (2003, 2007) and `http://deep.ps.uci.edu/DR4/home.html`; 7- Shectman et al. (1996) and `http://qold.astro.utoronto.ca/lin/catalog/lcrscat.tar.gz`; 8- Comparat et al. (2016); 9- Momcheva et al. (2016) and `http://3dhst.research.yale.edu/Data.php`; 10- Garilli et al. (2014) and `http://vipers.inaf.it/rel-pdr1.html`; 11- Garilli et al. (2008); Le Fèvre et al. (2004); 12- Yuan et al. (2015); 13- Lilly et al. (2009); 14- Ahn et al. (2014); 15- Driver et al. (2011); 16- `http://mur.ps.uci.edu/cooper/ACES/zcatalog.html`; 17- `http://apm5.ast.cam.ac.uk/arc-bin/wdb/aat_database/observation_log/make`; 18- Lidman et al. (2016) and `http://cosmosdb.iasf-milano.inaf.it/XXL/`; 19- Rest et al. (2014); Scolnic et al. (2014); Kaiser et al. (2010); 20- `http://www.nottingham.ac.uk/astronomy/UDS/UDSz/`; 21- Bazin et al. (2011) Private communication; 22- Mao et al. (2012); 23- Muzzin et al. (2012); 24- Sullivan et al. (2011); 25- Treu et al. (2015) and `https://archive.stsci.edu/prepds/glass/`; 26- Lidman et al. (2013); 27- Silverman et al. (2015) and `http://member.ipmu.jp/fmos-cosmos/FC_catalogs.html`; 28- Tasca et al. (2016) and `http://cesam.lam.fr/vuds/DR1/`; 29- `http://mosdef.astro.berkeley.edu`; 30- Stalin et al. (2010).

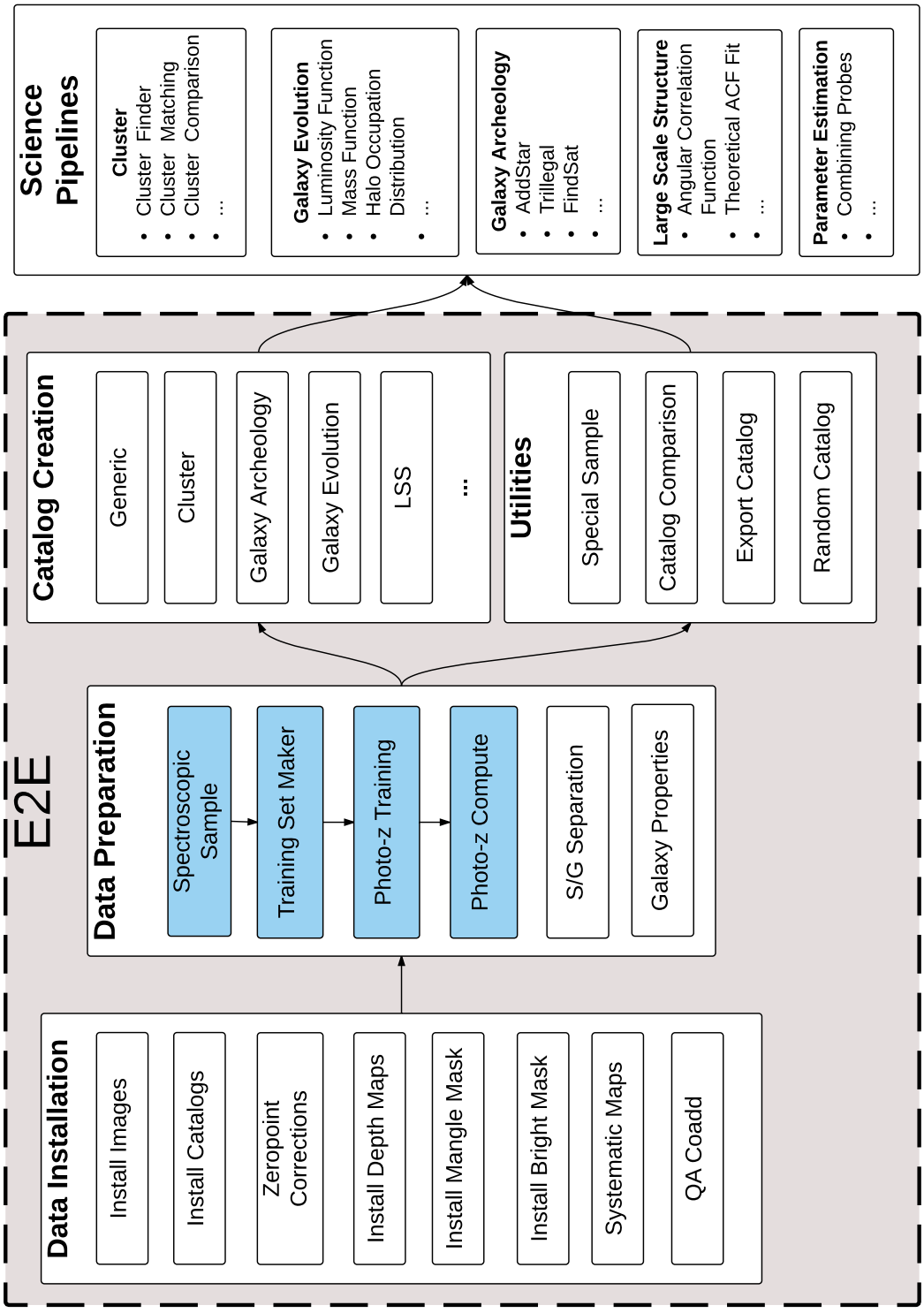

Figure 4: Diagram with some of the Portal pipelines. Those directly involved in the photo-z production are highlighted in blue. The gray dashed area delimits the E2E process, the group of pipelines needed to create catalogs.

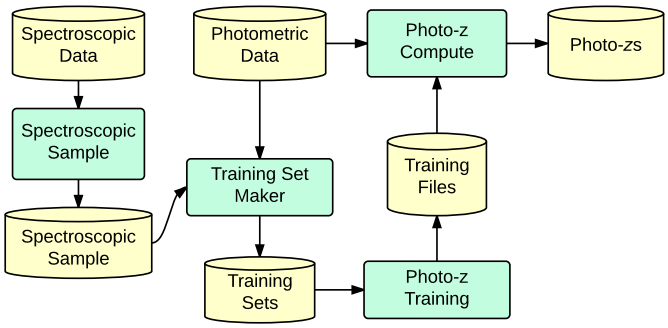

Figure 5: Steps followed in going from the original photometric and spectroscopic samples to the photo-z estimation. In yellow, the tables stored in the database and the products related to photo-z calculation. In green, the pipelines involved: *Spectroscopic Sample* (Section 3.1), *Training Set Maker* (Sections 3.2 and 3.3), *Photo-z Training* (Section 3.4), and *Photo-z Compute* (Section 3.5).

3.1. Defining a spectroscopic sample

Empirical algorithms require a sample of known redshifts to train themselves. For observed data, it is common to trust in spectroscopic redshifts as true values, due to their smaller uncertainties in comparison to photo-zs. In our case, we firstly define a spectroscopic sample which is later matched to the photometric data of interest to build training and validation sets. Figure 6 shows the Portal interface of the pipeline *Spectroscopic Sample*, as explained above. The supplemental video V1[5] shows an example of a run using the *Spectroscopic Sample* pipeline and a quick exploration of its results.

In particular, the Portal is used to upload the spectroscopic data available in the literature. To map the different quality flags adopted by individual authors, the Portal uses the following standard: $Q_{spec} = 1$ (no spec-z), $Q_{spec} = 2$ (low confidence on redshift), $Q_{spec} = 3$ (good confidence on redshift), and $Q_{spec} = 4$ (secure redshift). As distinct surveys have their own quality criteria, we created a table to convert the redshift quality flags, on a best effort basis, from the surveys we use to the system adopted in OzDES redshift survey (Yuan et al., 2015). The database associated with the Portal serves as a centralized spectroscopic database for DES, being continually updated, in particular by ongoing follow-up observations from DES collaborators such as the OzDES collaboration.

We identify multiple observations of the same object by selecting galaxies of all surveys that are within a user-specified search radius, here taken to be 1 arcsec. We have implemented two possible procedures to handle multiple measurements: the first consists of averaging all redshifts for the same source to produce a mean redshift; the second method, which we use in this work, chooses the best redshift with the following criteria. We first try to select the measurement that has the highest Q_{spec}. If more than one observation has the same Q_{spec} flag, we select the one that was observed more recently. If there were two or more observations in the same year, we choose the redshift with the smallest error, when it is available (not all surveys provide spec-z errors). Finally, if we still have more than one source (from the same year and with no errors available), we choose the one closest to the mean value of all the multiple measurements. Since we have selected a high "quality" threshold, the differences between choosing the best source or averaging between all the different matches are negligible.

Applying the above criteria to the database we create a spectroscopic sample containing high-quality measurements of redshifts from extragalactic objects, which is used below in the construction of training sets.

3.2. Matching spectroscopic and photometric samples

Once the spectroscopic sample is defined, the next step is to match the photometric data with the spectroscopic catalog containing the known and precise redshifts.

The *Training Set Maker* pipeline builds training sets by combining photometric sample(s) chosen by the user, among the datasets defined in the previous section, with a spectroscopic sample, which comes from the *Spectroscopic Sample* pipeline. When running *Training Set Maker*, the user must choose a spectroscopic sample (*Targets* menu), one or more photometric dataset(s) (in the tab *Object Catalog*). Optionally, it is possible to apply zero-point corrections in the observed magnitudes, like galactic extinction and stellar locus regression calibrations (High et al., 2009).

The matching is done based on the angular separation between the objects in the spectroscopic and photometric catalogs. We have selected the radius to 1.0 arcsec as a default configuration, after examining the distribution of the nearest (photometric) neighbor to each spectroscopic source in Y1A1 (see Figure 7). About 99% of the matches have separations ≤ 0.5 arcsec. If two or more objects are within the search radius, the nearest photometric object to the spectroscopic one is selected. This step is done directly in DES Science Portal database, using a PostgreSQL extension for spatial indexing on a sphere, called Q3C (Koposov and Bartunov, 2006). The supplemental video V2[6] shows a live run example of the pipeline *Training Set Maker*, using the spectroscopic sample created in the previous step.

In the fourth column of Table 1, we show the number of matched objects by the photometric dataset. We find 82,797 and 32,482 sources for the combined D04+S82 sets and the DFULL set respectively. Different combinations of these datasets resulted in the training and validation sets used in this paper.

3.3. Creating training and validation sets

Ideally, the training sample should have the same properties as the photometric sample of interest. However, this is difficult to meet when spectroscopic data come from surveys with different depths, redshift intervals, and targeting strategies distinct samples of galaxies. Different training sets have been

[5] https://youtu.be/1mu-PqOvK88?list=PLGFEWqwqBauBIYa8H6KnZ4d-5ytM59vG2

[6] https://youtu.be/2nA1PFGCnEM?list=PLGFEWqwqBauBIYa8H6KnZ4d-5ytM59vG2

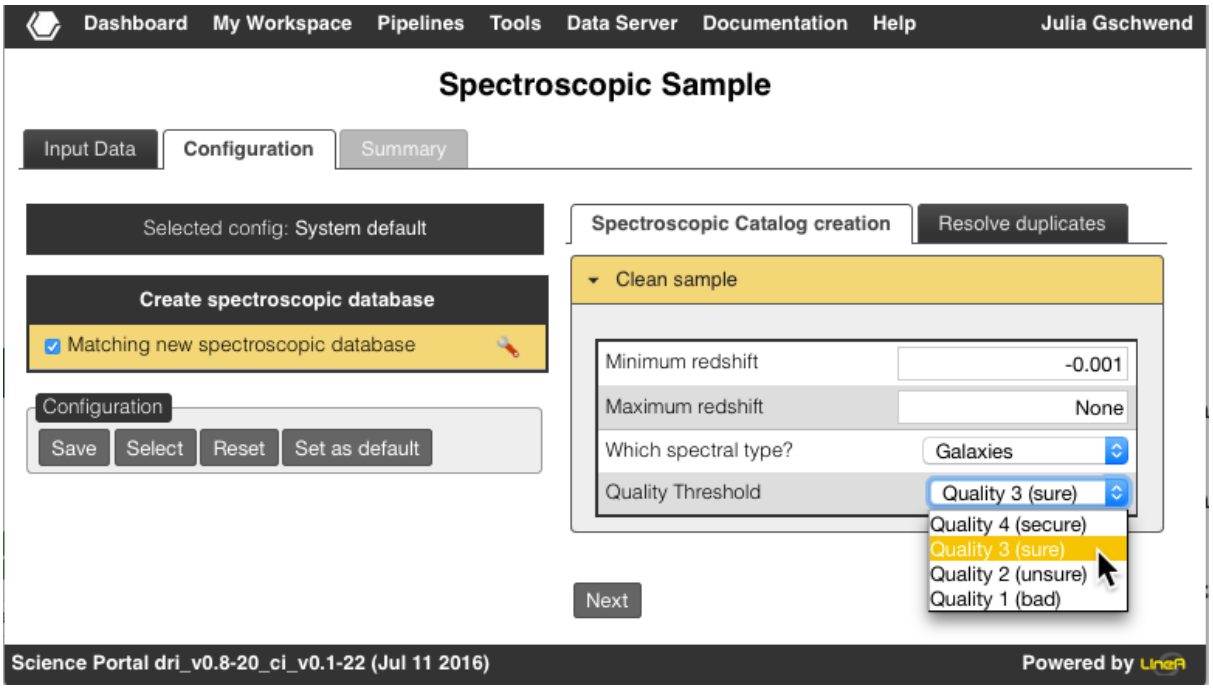

Figure 6: Screenshot of the *Configuration* tab of the *Spectroscopic Sample* pipeline. In this tab, the user makes decisions about spec-z quality and the criterion to resolve duplicates.

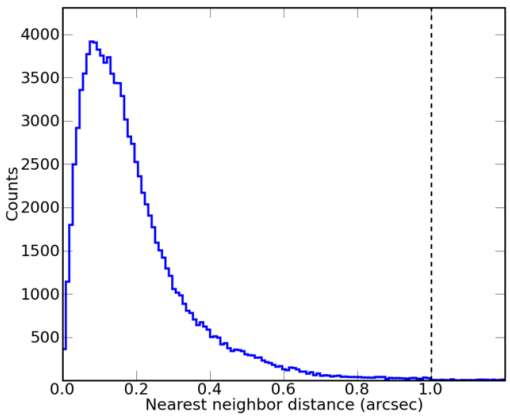

Figure 7: Distribution of distances between spectroscopic sources and their nearest photometric neighbor in DES Y1A1. 99% of the matches occur for separations ≤ 0.5 arcsec. In our analysis we set a maximum search radius of 1 arcsec (dashed line).

built to investigate possible effects in the estimated redshifts caused by these mismatches. Due to the flexibility of the *Training Set Maker* pipeline, one can quickly create several training sets, keeping full control of versions and configurations used for each one of them.

In this paper, we consider four training sets with different properties, built from the matched catalog just mentioned. One important aspect of photo-zs is the quality assessment of the training solution provided by the photo-z algorithms. To quantify this, we validate the training network on a test sample with known redshifts. We created validation sets using two approaches. The first one is the division of the matched catalog in two, where one part is used for training and the other for validation. The second one is to use the complete matched catalog for training and validate the photo-zs using independent samples with photometric properties different from those of the training sets, as previously done by Bonnett et al. (2016).

The first method is the default case in the *Science Portal Configuration*. Here we set the training and validation subsets to have the same size, randomly splitting the original catalog into two halves (Table 3). This approach is a compromise between having a large enough training set as well as adequate statistics to estimate the quality of the computed photo-zs. However, the second approach is critical since, for practical cases, the distributions of magnitudes, colors, and redshift of photometric samples and training sets do not entirely coincide.

The training and the default validation samples used in this paper are presented in Table 3, which lists the number of objects in each of the training and validation sets, together with an assigned number that we will use in the paper. The last column

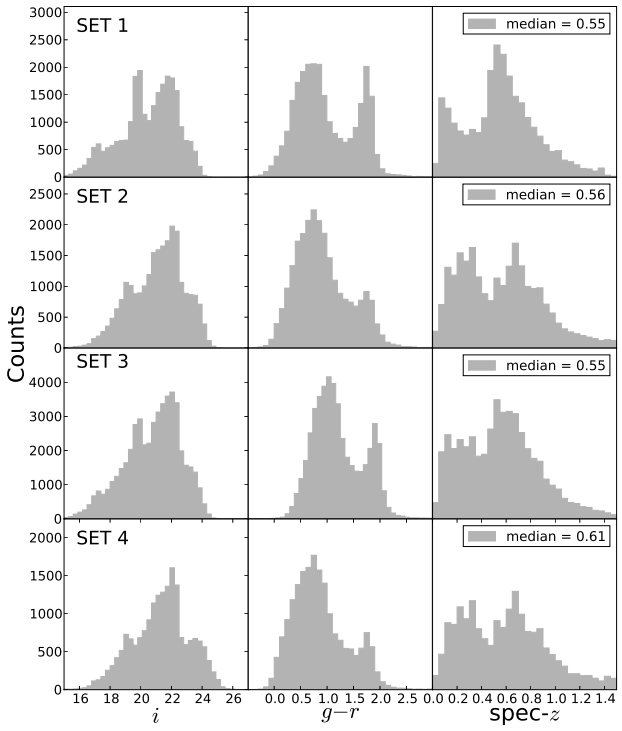

Figure 8: Distributions of i magnitude (left panel), $g - r$ color (middle) and redshift (right) of the four training sets discussed in the text. The sets listed in the figure are those defined in Table 3.

Table 3: Number of objects in the different training and validation sets.

Set	Dataset	Train	Valid	Valid †	Removed
1	S82	25,354	25,354	22,276	12.1%
2	D04	24,480	24,481	18,951	22.6%
3	D04 + S82	49,834	49,835	41,341	17.0%
4	DFULL	19,046	19,046	14,121	25.9%

† Number of objects after selection of $i < 22.5$.

contains the percentage of galaxies removed from the validation set, after imposing a magnitude limit cut in $i < 22.5$. This value was chosen as it is, approximately, the magnitude limit of the Y1 data and our main interest is to validate the photo-zs for a magnitude-limited sample. The magnitude (i-band), color (g-r) and redshift (spec-z) distributions for the training sets are shown in Figure 8.

We further examine the quality of our photo-z using three independent sets. We have used a pencil-beam survey containing all types of galaxies (zcosmos, Lilly et al., 2009), and two wide surveys with different morphological composition: CMASS (Alam et al., 2015) containing early-type galaxies and WIGGLEZ (Parkinson et al., 2012) primarily late-type galaxies. In order to validate with independent samples new training sets are made based on set 2, but excluding the objects that are present in the validation sets, to avoid identical galaxies within the training and validation samples. Therefore, we create the sets 2Z, 2W and 2C to train the algorithms before validating with zcosmos, WIGGLEZ and CMASS respectively (see Table 4). The i-band magnitude, $g - r$ color and redshift distributions of the three independent validation sets are shown in Figure 9.

Table 4: Training and validation sets used for independent cases†.

Set	Train	Valid	Valid ‡	Removed
ZCOSMOS	40,231 (2Z)	4,798	4,466	6.9%
WIGGLEZ	48,950 (2W)	10,608	10,410	1.9%
CMASS	48,956 (2C)	10,699	10,663	0.3%

† Spectroscopic matches with photometric DES Y1A1 data.
‡ Number of objects after selection of $i < 22.5$.

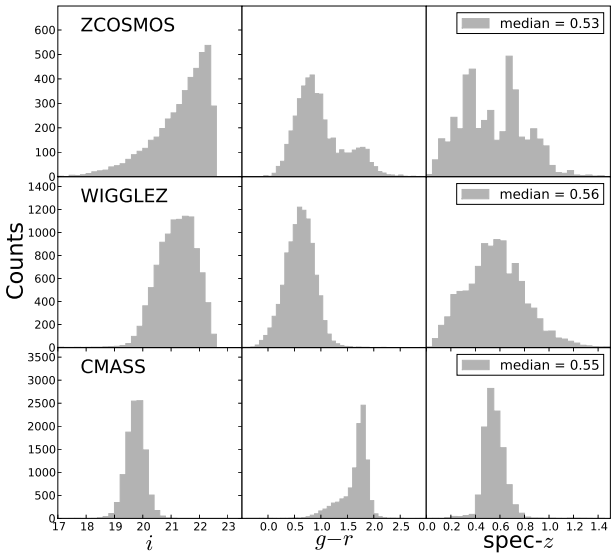

Figure 9: Same distributions as in Figure 8, but for the three independent (surveys that do not take part of training procedure) validation sets, ZCOSMOS, WIGGLEZ and CMASS. The sets listed in the figure are those defined in Table 4.

In summary, in this section, we have created four different training sets (and their respective validation sets), and three independent samples, ZCOSMOS, CMASS, and WIGGLEZ (which needed a modified version of set 2 for training).

3.4. Training and validating photo-z algorithms

In recent years the number of photo-z algorithms has increased enormously, and it is beyond the scope of the present paper to make a comprehensive review of the available algorithms. So far, the following codes are implemented in the Portal: ANNZ, ANNZ2, ARBORZ, DNF, LEPHARE, POFZ, SKYNET, and TPZ. Almost all algorithms are empirical methods, with the exceptions of LEPHARE, a template fitting code, for which a training sample can be used to improve photo-z through systematic shifts in the theoretical magnitudes from the spectral energy distribution (SED) templates.

Regarding the results shown in Section 4, for TPZ we used magnitudes and colors to build 200 trees, and considered the mean of the PDF as the photo-z single value. DNF was used in the Euclidean Neighborhood Fitting (ENF) mode, accepting

only magnitudes as observables, which is the faster mode but is not necessarily the one that provides the best results. For LePhare, the template library adopted was a subset with 21 SEDs, from elliptical to starburst galaxies, from the CFHTLS library. We applied the internal extinction from Prévot et al. (1984) with values of $E(B-V) = [0.0, 0.1, 0.2, 0.3]$. For the other algorithms, the configuration was the default for each code.

The codes mentioned above are implemented in the Portal in two separate pipelines shown in Figure 5. First, in *Photo-z Training*, where the training and validation steps are done. Second, in *Photo-z Compute*, where the products of the previous step, hereafter training files, are inherited and applied to compute photo-zs for large photometric samples.

The *Photo-z Training* pipeline consists of three components: "Subsets Separation", "Photo-z Training", and "Photo-z Validation".

In the "Subsets Separation" component, the user can define the sample selection criteria, choosing the acceptable intervals of magnitude, redshifts, colors and magnitude signal-to-noise ratio. Also, this component splits the matched catalog into two parts. The fraction of data used for training (and consequently the remaining fraction for validation) is a free parameter in the component's configuration. If the fraction is chosen to be 1.0, the validation step is skipped, and the whole sample is employed for training.

The "Photo-z Training" creates the training files, as well as registers the code configurations that will be applied to the next pipeline, *Photo-z Compute*. A unique training procedure can be used in the photo-z calculation for different photometric datasets.

The last component, "Photo-z Validation", produces quality assessment plots and validation metrics for all the selected codes, utilizing the same training files that will be used in the *Photo-z Compute* pipeline. An example is presented in Figure 10, showing the "Result" screen of the *Photo-z Training* pipeline, with "Validation Plots" for DNF algorithm. In the top menu, the user can navigate through tabs, to explore the results from different components.

An example of usage of the *Photo-z Training* pipeline is shown in the supplemental video V3[7]. There we apply the matched catalog created in the previous pipeline, *Training Set Maker*, to perform training and validation procedures with random halves of the sample. We also make a tour in the results screen to explore the metrics and diagnostic plots generated.

To assess the performance of the photo-z algorithms, we estimate metrics to quantify dispersion, systematic errors, and the capability of recovering the $N(z)$ distribution. We selected four from the ten metrics addressed in the DES science verification analysis. The equations that define these quantities are found in Sánchez et al. (2014). Below we describe the meaning of each one:

- *bias* is defined as the mean difference between photo-zs and spec-zs, quantifying some possible systematic trend of the photo-z to be larger or smaller than the spec-z. In the figures, we show a dotted line in the level 0.0 to make this trend more evident for the reader.

- σ_{68} is the half width of the distribution, with respect to the median of bias, where 68% of the date are enclosed (note that for Gaussian errors, this coincides with the standard deviation). This metric reflects the photo-z scattering around the expected values (spec-zs).

- $frac(> 2\sigma)$ is the fraction of catastrophic photo-zs that lie out of the interval of 2 times the standard deviation of the mean bias. This is another way to quantify the dispersion around the expected values.

- $\mathbf{N}_P$ measures the difference between the estimated N(photo-z) and the N(spec-z) for each bin, normalized by Poisson fluctuations $\sqrt{N(\text{spec}-z)}$. The global N_P is computed as the RMS of the values in redshift the intervals studied. This metric is a straightforward way to compare the two histograms that represent N(photo-z) and N(spec-z). N_P would be ideally equal 0.0 if both distributions coincide, so the level 0.0 is marked in the plots as a reference.

In Section 4 we adopt the same performance targets used by Sánchez et al. (2014), as a benchmark to compare different codes or training/validation sets. All those quantities are calculated globally and as a function of redshift, in intervals of 0.1. The goal of this comparison is to show that the Portal can be utilized as a tool to verify whether the data meet or not the scientific requirements, whatever they are. The Sánchez et al. (2014) benchmarks were formulated by DES collaboration as pre-survey estimates of photo-z performance needs. Subsequent experience and analyses have led to a substantial and ongoing evolution in the types of statistics taken to verify that photo-z errors do not contribute significantly to the cosmological error budgets. Science requirements for some specific studies have to be more strict, e.g., tomographic weak lensing studies (Bonnett et al., 2016), and driven by the scientific case of interest.

The *Photo-z Training* pipeline presents the metrics automatically if the validation step is performed. Errors in the metric values are estimated using the Bootstrap re-sampling technique (Bradley and Tibshirani, 1993) based on 100 realizations, as done in Sánchez et al. (2014). We recall that the main purpose of the *Photo-z Training* pipeline is the creation of the training solutions for multiple algorithms, and the automatic validation of them, before their application to the photometric sample. In Section 4 we summarize the results we have obtained for the different training and validation samples presented in Section 2, as an example of how DES Science Portal can aid to assess the photo-z performance of different codes and configurations.

3.5. Computing Photo-zs for large datasets

The actual photo-zs calculation in DES Science Portal is done through the *Photo-z Compute* pipeline. This pipeline estimates photo-zs for all co-added objects present in the photometric sample, regardless of the object's nature (e.g., star or

[7] `https://youtu.be/ZOJ0hGWlvag?list=PLGFEWqwqBauBIYa8H6KnZ4d-5ytM59vG2`

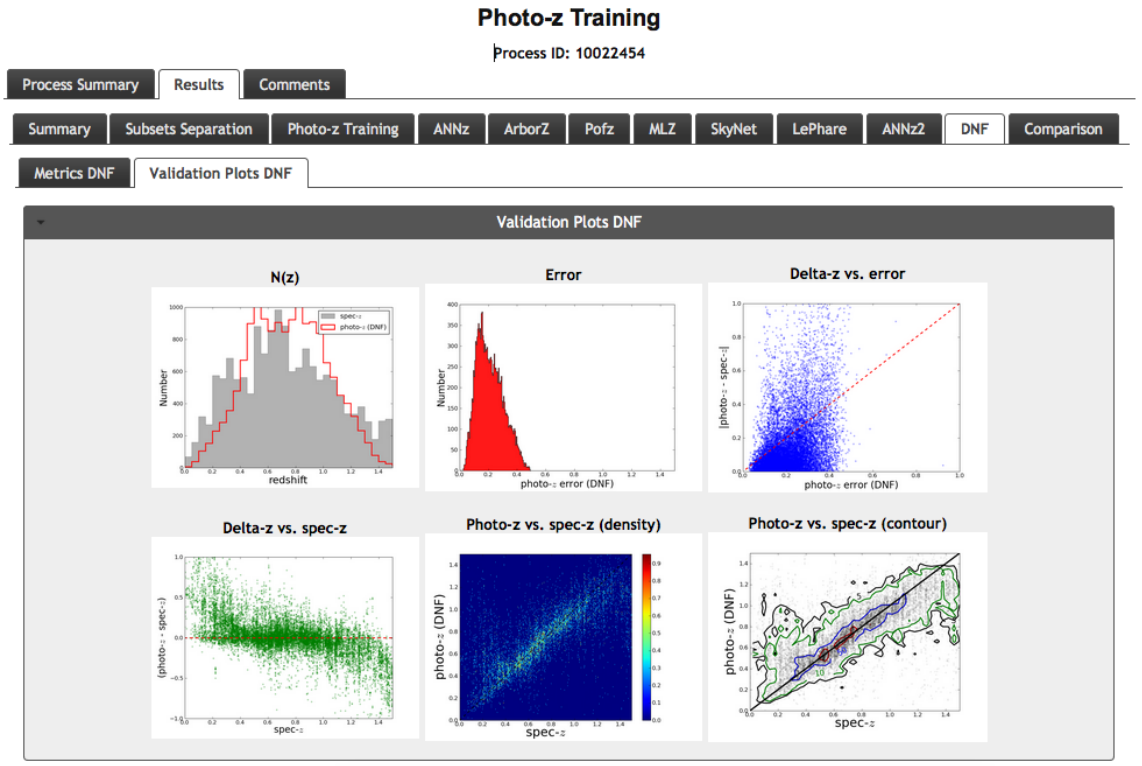

Figure 10: Results from the *Photo-z Validation* component, organized in tabs by photo-z algorithms. In this case, we present results for DNF algorithm.

galaxy). Once the photo-zs are calculated, they will be utilized to aid in the creation of catalogs ready for Portal science workflows, considering, e.g., different star/galaxy classifiers, color cuts, and magnitude limits.

Since the same object can be tagged as galaxy by one classifier or star by another, it is important to have photo-zs available for all objects. Therefore, the $N(z)$ obtained with the *Photo-z Compute* pipeline is not representative of the true galaxy distribution yet, and only when the final catalogs are produced, that the $N(z)$ can be used for scientific analyses.

Photo-z Compute is the most computationally intensive of all the photo-z related pipelines. As we need to deal with the entire photometric sample, to do so efficiently, data access happens through Hadoop[8] File System. The pipeline allows two types of parallelization procedures, depending on the code. TPZ, for instance, has an implementation based on Message Passing Interface (MPI), so we deploy only one thread (a DES tile of about 0.5 deg^2) per node and MPI itself fills all the cores in that node. On the other hand, DNF and other codes have several threads executed per node, each occupying a core (typically 24 cores per node on our production cluster). These threads are consolidated and ingested in the database. More details about parallelization and benchmarks will be presented elsewhere (Fausti et al. 2017, in preparation).

We show an example of running the *Photo-z Compute* pipeline in the supplemental video V4[9]. There, we apply the training files created in the previous step and perform the photo-z calculation for the whole photometric dataset S82. We also show the resulting distribution of photo-zs, with the caveat that, at this stage, the star/galaxy classification was not performed yet.

4. Use case examples

In this section, we present and discuss some examples to illustrate the benefit of having an infrastructure as such. We show examples of tests carried out with the *Photo-z Training* pipeline, to explore different configurations that can later be used to calculate photo-zs for the photometric sample, using the *Photo-z Compute* pipeline. These tests show the versatility of the Portal in producing photo-zs in different scenarios. On the other hand, as previously stated, the photo-z estimations presented here have not been robustly validated by the DES photo-z working group, and are therefore not meant to be used in a scientific analysis.

For simplicity, in most of the tests, we only show the results obtained with TPZ and DNF algorithms. TPZ was chosen due to its good performance on previous DES Science Verification data (e.g., Sánchez et al., 2014). DNF, the nearest neighbor algorithm, for being computationally fast, especially in the ENF

[8] http://hadoop.apache.org/

[9] https://youtu.be/IcCk0MYhy-E?list=PLGFEWqwqBauBIYa8H6KnZ4d-5ytM59vG2

mode. A comparison with other codes installed at the Portal can be seen in Section 4.2.

4.1. Dependence on training sets

We start our examples by randomly splitting the training sets defined in Section 3.3 into two, with the same sizes, to be used for training and validation. In this case, the training sample is representative of the validation sample. To ensure the total coverage of magnitude and color ranges, by default no cuts were done in the training set. Nonetheless, for validation, all results presented here use validation sets limited to $i < 22.5$, which is brighter than the magnitude limit of all datasets considered.

To reveal the impact of constructing training samples in regions of the sky with different characteristics, we compare sets 1 and 2 (see Table 3). The results obtained with training sets 2 and 3 may help us understand the relevance of the training set size, and finally, comparing the results obtained with training sets 2 and 4 may be useful to assess the effect of signal-to-noise. While other training sets could conceivably be proposed, we believe that these four sets considered here span a wide range of possibilities.

We show the metrics in intervals of photo-z in Figure 11. The global values are summarized in Table 5. We note that the difference between metrics, especially bias, is much larger than the metric errors, which are statistical in nature.

The four pairs of training/validation sets provide very similar global metrics for most of the photo-z range. The discrepancies become significant only at high redshifts ($z \geqslant 1.0$). The *biases* are small for the two algorithms, at least up to $z \sim 0.8$. For σ_{68} both codes fulfill the pre-survey performance targets (< 0.12, marked by the dashed line), also up to $z \sim 1.0$. The fraction of outliers $frac(> 2\sigma)$ satisfies the requirement (< 0.1) for all the redshift range studied (see Table 5). For both algorithms, the smallest value of N_p (the best agreement) was obtained with set 4 (DFULL), where the signal-to-noise ratio of galaxies is better, even though the difference with set 2 is not large (its counterpart, D04).

Comparing sets 1 and 2, we do not see significant discrepancies in the value of N_p. It indicates that the differences in these two regions of the sky are not relevant for recovering the photo-z distributions. Finally, a comparison between sets 2 and 3 reveals that increasing the size of the training set does not necessarily produce improvements in the photo-z metrics either. The distributions of redshifts, shown in the right panel of Figure 11, are reasonably well recovered in all cases.

In this first example, we show that the photo-z distributions recover the spec-z distributions reasonably well when training and validation sets have similar photometric properties. Unfortunately, the spectroscopic sample available in the Portal's database does not resemble the photometric properties of Y1A1, regarding the distributions of colors and magnitudes. Therefore, the validation procedure used in these tests does not set the quality levels for the photo-zs calculated in DES. However, it is useful to make comparisons between different codes and their configurations, for better understanding the impact of decisions taken when building training sets.

Table 5: Global metrics for the validation sets composed by one half of matched catalogs, after training with the other half.

Algorithm	Set	*bias* $\times(10^{-4})$	σ_{68} $\times(10^{-4})$	$frac(> 2\sigma)$ $\times(10^{-4})$	N_P $\times(10^{-2})$
DNF	1	5 ±3	533±2	522±3	571±6
	2	83 ±3	638±2	513±4	611±8
	3	66 ±2	605±2	503±3	796±6
	4	126±4	542±2	498±5	514±7
TPZ	1	-74±3	518±2	491±3	745±5
	2	-58±3	602±2	463±4	638±6
	3	-58±3	574±1	465±3	856±7
	4	-17±4	490±2	446±4	429±5

Regarding the purpose of the tests presented in this section, we conclude that in the case of a representative training sample: (i) The different regions of the sky used to create training and validation sets shows no influence on the photo-z quality. It means that the regions that compose the datasets in Y1A1 are large enough to present similar depth in average and to be not substantially affected by the cosmic variance during the training procedure. (ii) The training set size does not affect much the results, as we are working with a training sample that is already representative of the validation sample. (iii) The differences in the signal-to-noise ratio of training sets 2 (D04), and 4 (DFULL) are not large enough to induce significant differences in their results.

4.2. Dependence on the photo-z algorithm

In this section, use the training set 2 to study the performance of all the photo-z algorithms currently installed in the Science Portal and how their performances compare to one another and in particular to TPZ and DNF. For further algorithm comparisons, we refer to Hildebrandt et al. (2010) and Carrasco Kind and Brunner (2014).

The set is validated using the validation sample representative of itself, but limiting at $i < 22.5$. The variation of metrics as a function of redshift interval is presented in the two first panels of Figure 12. Global metrics are shown in Table 6. Similar to the analysis presented in the previous section, here again, we compared the metrics with the pre-survey performance targets, as a benchmark to allow the comparison. In the third panel we show the comparison between the $N(z)$s, from photo-zs and spec-zs.

These results indicate that nearly all codes have similar behavior, except close to the limits of the redshift range considered. Besides SKYNET and POFZ, all the other codes lead to similar results but with TPZ in general yielding slightly better results. However, DNF is by far the fastest code available while TPZ and LEPHARE are the slowest. Approximately, they all meet the collaboration pre-survey performance targets, although TPZ and DNF do seem to behave slightly better, therefore justifying our choice to use them in the more detailed tests.

For most of the cases, the algorithms were run in the default mode. It is possible that the results can be improved if we investigate the impact of the configuration parameters for each one of the photo-z codes available. For instance, POFZ, LEPHARE, and SKYNET, which show here the larger differences in

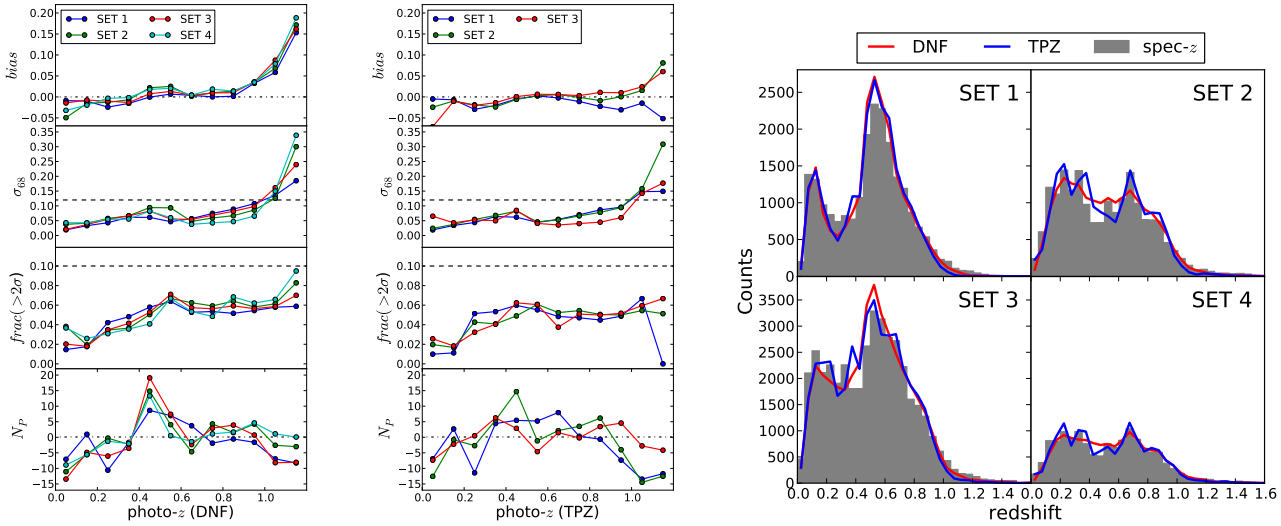

Figure 11: Left and middle panels: the variation of metrics in redshift intervals computed by the comparison between the photo-z estimated by DNF (left) or TPZ (middle) and spec-zs for the validation sets described in Table 3. The dotted horizontal lines indicate the level 0.0. The dashed horizontal lines indicate the pre-survey performance targets for the global metrics, here useful to guide the eyes through the metric's behavior as a function of redshift. Right panel: distributions of the estimated photo-z by DNF (red line), TPZ (blue line) and spec-z (fulfilled gray histogram) for validation sets 1 through 4.

Table 6: Global metrics for all photo-z codes using the set 2.

Algorithm	*bias* $\times(10^{-4})$	σ_{68} $\times(10^{-4})$	*frac*$(>2\sigma)$ $\times(10^{-4})$	N_P $\times(10^{-2})$
ANNZ	135±4	750±3	466±4	1061±9
ANNZ2	90±3	782±2	469±3	1046±9
ARBORZ	254±4	656±2	488±4	1018±8
DNF	83±4	638±2	513±4	611±8
LEPHARE	321±5	941±3	514±4	1277±695
POFZ	-469±5	1087±4	521±3	1436±16
SKYNET	438±4	1164±7	596±3	1156±7
TPZ	-58±3	602±2	463±4	638±6

the reproduced $N(z)$ distribution, performed better in Sánchez et al. (2014). Therefore, despite this analysis does not assess the realistic metrics for Y1, the results presented in Table 6 show the capability of the Portal to make fair comparisons between methods, ensuring the same conditions in their execution.

4.3. Validation with independent sets

The ways of evaluating the quality of computed photo-zs described earlier suffers the weakness that the validation samples are similar to the sample used for the training which, of course, is not usually the case. Weighting the validation sample, so that it takes into account the magnitude and color distributions of the photometric sample of interest, is a way to tackle this problem.

Another more direct way is to validate the estimated photo-zs using a sample that is independent from that used in training, to see whether the codes are capable of recovering a redshift distribution whatever it is. We start doing that using the spectroscopic sample of zCOSMOS (Lilly et al., 2009) to create an independent validation set.

Table 7: Global metrics evaluated in zCOSMOS independent validation set, after training with training set 2C.

Algorithm	*bias* $\times(10^{-4})$	σ_{68} $\times(10^{-4})$	*frac*$(>2\sigma)$ $\times(10^{-4})$	N_P $\times(10^{-2})$
DNF	164±5	714±7	530±9	654±11
TPZ	25±6	663±4	502±9	500±10

Here, we show the results obtained using the training set 2Z listed in Table 4 of Section 3.3. The results are shown in Figure 13 and summarized in Table 7 for photo-zs obtained using the DNF and TPZ codes. As can be seen in the figure, both codes lead to very similar results with the usual metrics satisfying the pre-survey performance targets over a large range of redshifts. For redshifts greater than 0.8, the bias becomes slightly positive (DNF) or negative (TPZ), before it starts to increase systematically beyond $z = 1$.

We compare the computed photo-zs to the measured redshift distribution in the right panel of Figure 13. It is remarkable that the sharp features of the very inhomogeneous distribution which characterize this pencil-beam survey are reasonably reproduced, including the location of the peaks in the case of TPZ.

Both DNF and TPZ provide not only a single estimation for the photo-z, but also a probability density function (PDF) over the redshift range regarded. For simplicity, we decided to show in this paper only the $N(z)$ using the single photo-z values.

To understand the effect of the predominance of a particular galaxy type in the sample, we have also used as independent samples WiggleZ and CMASS. Based on their color distributions, we infer that the first almost exclusively composed by late-type galaxies, whereas the second is dominated by early-type galax-

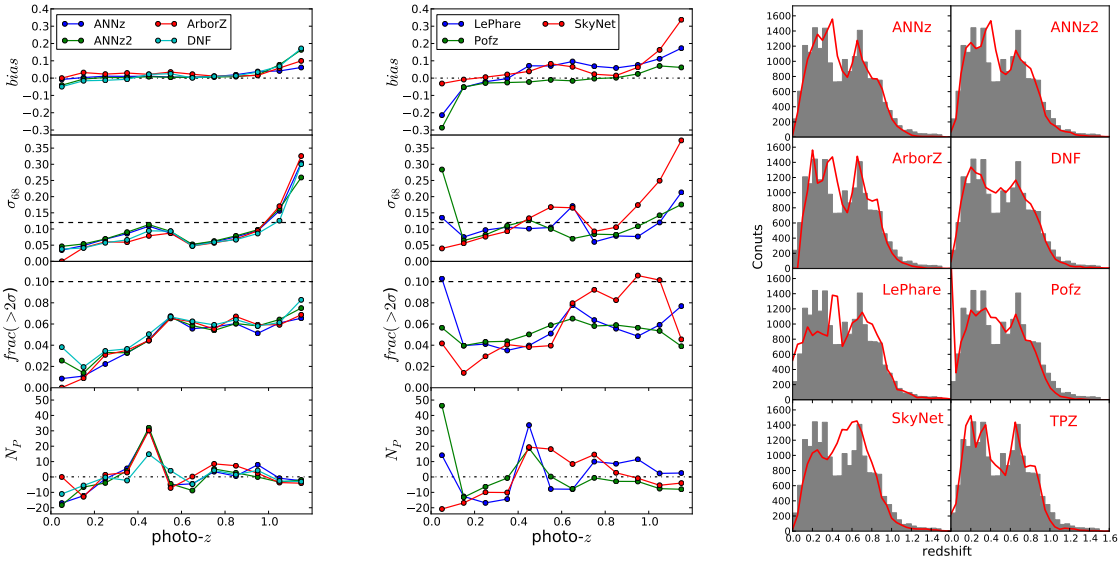

Figure 12: First and second panels: The variation of metrics in redshift intervals for photo-zs estimated by all photo-z codes validated in set 2 and limited to $i < 22.5$, after training with set 2. The dotted horizontal lines indicate the level 0.0. The dashed horizontal lines symbolize the pre-survey performance targets for the global metrics, as a benchmark to allow the comparison. Third panel: Comparison between the estimated photo-z (lines) and spec-z distributions (fulfilled histogram) for all photo-z codes, trained on the training set 2 and applied to the corresponding validation set 2 limited at $i < 22.5$.

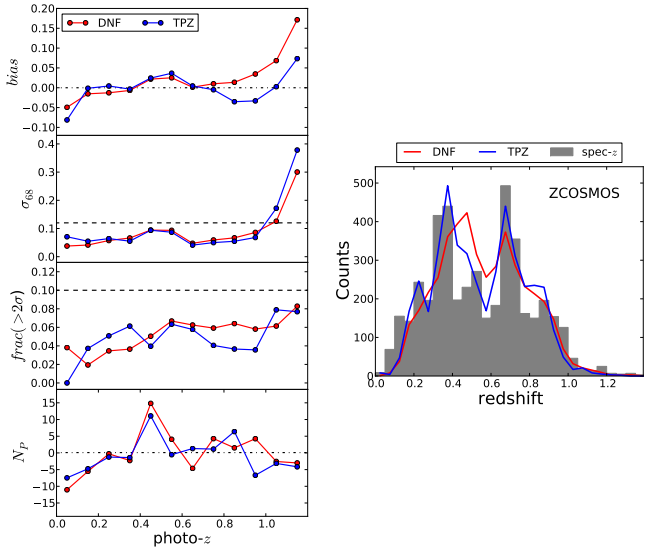

Figure 13: Left: the variation of metrics as a function of redshift comparing the photo-z estimated with DNF or TPZ and the spec-zs for zCOSMOS. The dotted horizontal lines indicate the level 0.0. The dashed horizontal lines represent pre-survey performance target for the global values. Right: comparison of the photo-z (lines) and spec-z (fulfilled gray histogram) distributions. In red, the results obtained with DNF, and in blue with TPZ.

ies. The results for WIGGLEZ and CMASS samples were obtained using the DNF and TPZ codes and the training sets listed in Table 4.

While the redshift distribution of early-type galaxies is reproduced extremely well, this is not the case for late-types especially in the interval $0.2 < z < 0.7$. Two factors contribute to the best performance of photo-z codes in CMASS. First, the nature of the early-types' SED, with the remarkable feature around 4000 Å, which makes easier the determination of the photo-zs when there are only five bands available, as the DES case (e.g., Budavári et al., 2001). Second, the absence of objects at lower redshifts, where the lack of the u-band has the significant impact.

Altogether, the results from Sections 4.1 to 4.3 indicate that the Portal infrastructure is ready to compute photo-zs and can be used as a tool to perform a wide range of tests. The determination of the best method or the best training and validation samples for Y1A1 and future releases are a good example. These results are particularly important, for instance, for cluster finders based on photo-zs such as WAZP (Benoist et al. 2017, in preparation), or for the calculation of luminosity and stellar mass functions, both science pipelines currently under implementation in the Portal.

4.4. Tests on Y1A1 data

We have used training set 2 to compute photo-zs for the objects in the S82, the larger region considered in this work, using the DNF and TPZ codes. The results are shown in Figure 15. We should emphasize that photo-zs were computed for all objects without any color or magnitude cuts, nor classification. The time spent to run *Photo-z Compute* was approximately 1.2

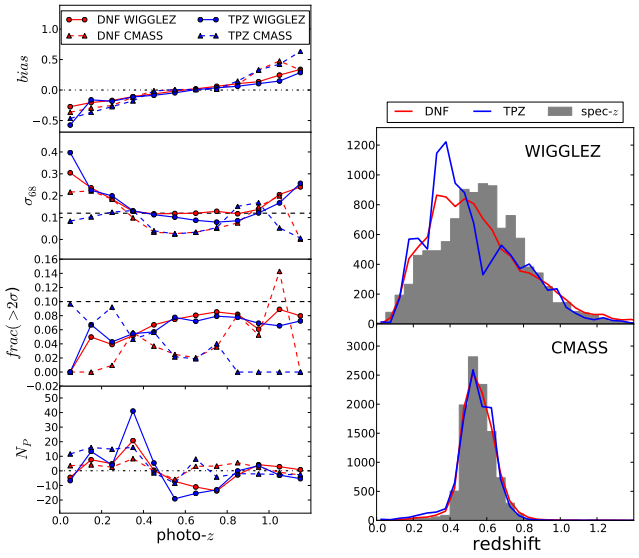

Figure 14: Left: the variation of metrics as a function of redshift comparing the photo-z estimated with DNF or TPZ and the spec-zs for WIGGLEZ and CMASS. The dotted horizontal lines indicate the level 0.0. The dashed horizontal lines represent pre-survey performance target for the global values. Right: the comparison of the photo-z and spec-z distributions for WIGGLEZ (top) and CMASS (bottom), obtained with DNF (red), and TPZ (blue).

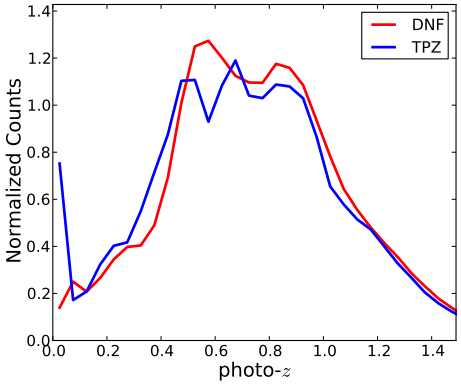

Figure 15: Photo-z distribution for the S82 field, measured by *Photo-z Compute* pipeline, after training with set 2. At this stage, there is neither quality pruning nor star/galaxy classification, so this distribution does not reflect the real galaxy $N(z)$.

minutes per million objects for DNF and 6.5 minutes per million objects for TPZ, using the parallelization described in section 3. Even though it takes more time to compute photo-zs for a larger sample that was not pruned, later it provides greater flexibility and speed when producing catalogs ready for Portal science-workflows, as one does not have to go back and re-run *Photo-z Compute* if different pruning decisions are made. Besides, regarding star/galaxy classification choices, the number of stars in DES footprint is much smaller than that of galaxies (since we are avoiding the Galactic disk) so keeping stars in the photometric sample does not add much to photo-z computation time.

External tests using the SPT region, which is even larger than S82 (see Figure 1), revealed that the features seen in the distributions are characteristics of the code and not the region, as the distributions obtained for the two regions are almost identical. We note that the rise in the number of objects with TPZ photo-z close to zero is mostly related to stars (98%), as classified by `MODEST` method (e.g., Chang et al., 2015) which is based on the `SPREAD_MODEL` parameter (Desai et al., 2012) (see also DES Y1 release paper in preparation).

5. Summary

In this paper, we have described the infrastructure available in the Science Portal to create training sets, training files and to compute photo-z using different algorithms. It is an easy-to-use framework that concatenates all the different pipelines involved in the calculation of photo-zs, ensuring consistency between these processes. The pipeline used in the estimation of photo-zs is parallelized to improve performance. Since all processes are registered in a database, the Portal framework eases the task of carrying out a large variety of tests and comparing the results as illustrated in the present paper. Also, the infrastructure is used as a first step in the preparation of catalogs ready for Portal science workflows.

Once training sets are prepared, photo-zs obtained from all codes of interest are calculated and stored in tables which can later be used as input in the preparation of science catalogs.

New spectroscopic data are continuously ingested into the database associated with the Portal, increasing the number of entries used in the construction of training and validation sets. Even though the redshift repository continuously grows, the list of surveys used in any test is reported and registered, so the test can be reproduced in the future, using only the surveys of interest.

Considering the volume of data, the number of algorithms and the number of releases of new photometric and spectroscopic data, having a structured framework like the one presented here is critical for the vetting of DES algorithmic improvements, and the systematic production of photo-z's for future DES releases.

As an example, we used the available Portal infrastructure on DES Y1 data, evaluating in different ways the quality of computed photo-zs using different training sets and algorithms. The realistic validation set that will give a precise prediction of the photo-z quality for Y1 is the subject of another paper that is being prepared by the collaboration. Here, we show a list of comparative tests that gives us several clues about the photo-z quality for Y1A1, besides it makes evident the Portal's flexibility to perform a large variety of tests.

It is important to point out that the strategy adopted by the Portal is to compute photo-zs for all objects in the original catalog produced by DESDM. We do that because the photo-z calculation is, by far, the most computationally intensive step of the E2E process. Calculating photo-zs for all objects gives the flexibility to create any catalog for Portal science workflows without having to re-compute photo-zs if one decides to change the star/galaxy classifier or the sample selection. One disad-

vantage of our approach is that, in this first pass, we only compute point-values of photo-z. The calculation of a full PDF happens at a later stage when the number of objects of interest is smaller, after quality pruning and star-galaxy separation. This will be discussed in a separate paper that focuses on the method of preparing catalogs ready for Portal science workflows.

Finally, we would like to mention that, recently, the entire Portal framework was adapted to handle with simulations, besides the observed data. It represents a significant increase in the number of applications of the Portal in future scientific analysis.

Acknowledgments

We thank P. Egeland and F. Ostrovski for the contribution in the early phases of development of this infrastructure. We also thank R. Brito, J.G.S. Dias, V. Machado, L. Nunes, and G. Vila Verde for the contributions in the Portal's basic infrastructure, essential for the realization of this work.

JG is supported by CAPES. ACR is supported by CNPq process 157684/2015-6. ML is partially supported by CNPq and FAPESP. Part of this research is supported by INCT do e-Universo (CNPq grant 465376/2014-2).

Funding for DES Projects has been provided by the U.S. Department of Energy, the U.S. National Science Foundation, the Ministry of Science and Education of Spain, the Science and Technology Facilities Council of the United Kingdom, the Higher Education Funding Council for England, the National Center for Supercomputing Applications at the University of Illinois at Urbana-Champaign, the Kavli Institute of Cosmological Physics at the University of Chicago, the Center for Cosmology and Astro-Particle Physics at the Ohio State University, the Mitchell Institute for Fundamental Physics and Astronomy at Texas A&M University, Financiadora de Estudos e Projetos, Fundação Carlos Chagas Filho de Amparo à Pesquisa do Estado do Rio de Janeiro, Conselho Nacional de Desenvolvimento Científico e Tecnológico and the Ministério da Ciência, Tecnologia e Inovação, the Deutsche Forschungsgemeinschaft and the Collaborating Institutions in the Dark Energy Survey.

The Collaborating Institutions are Argonne National Laboratory, the University of California at Santa Cruz, the University of Cambridge, Centro de Investigaciones Energéticas, Medioambientales y Tecnológicas-Madrid, the University of Chicago, University College London, the DES-Brazil Consortium, the University of Edinburgh, the Eidgenössische Technische Hochschule (ETH) Zürich, Fermi National Accelerator Laboratory, the University of Illinois at Urbana-Champaign, the Institut de Ciències de l'Espai (IEEC/CSIC), the Institut de Física d'Altes Energies, Lawrence Berkeley National Laboratory, the Ludwig-Maximilians Universität München and the associated Excellence Cluster Universe, the University of Michigan, the National Optical Astronomy Observatory, the University of Nottingham, The Ohio State University, the University of Pennsylvania, the University of Portsmouth, SLAC National Accelerator Laboratory, Stanford University, the University of Sussex, Texas A&M University, and the OzDES Membership Consortium.

The DES data management system is supported by the National Science Foundation under Grant Number AST-1138766. The DES participants from Spanish institutions are partially supported by MINECO under grants AYA2015-71825, ESP2015-88861, FPA2015-68048, SEV-2012-0234, SEV-2012-0249, and MDM-2015-0509, some of which include ERDF funds from the European Union. IFAE is partially funded by the CERCA program of the Generalitat de Catalunya.

Parts of this research were conducted by the Australian Research Council Centre of Excellence for All-sky Astrophysics (CAASTRO), through project number CE110001020.

This paper has gone through internal review by DES collaboration.

References

Abazajian, K.N., Adelman-McCarthy, J.K., Agüeros, M.A., et al., 2009. The Seventh Data Release of the Sloan Digital Sky Survey. ApJS 182, 543–558. doi:10.1088/0067-0049/182/2/543, arXiv:0812.0649.

Abbott, T., Abdalla, F.B., Allam, S., Dark Energy Survey Collaboration, 2016. Cosmology from cosmic shear with Dark Energy Survey Science Verification data. Phys. Rev. D 94, 022001. doi:10.1103/PhysRevD.94.022001.

Ahn, C.P., Alexandroff, R., Allende Prieto, C., et al., 2014. The Tenth Data Release of the Sloan Digital Sky Survey: First Spectroscopic Data from the SDSS-III Apache Point Observatory Galactic Evolution Experiment. ApJS 211, 17. doi:10.1088/0067-0049/211/2/17, arXiv:1307.7735.

Alam, S., Albareti, F.D., Allende Prieto, C., et al., 2015. The Eleventh and Twelfth Data Releases of the Sloan Digital Sky Survey: Final Data from SDSS-III. ApJS 219, 12. doi:10.1088/0067-0049/219/1/12, arXiv:1501.00963.

Arnouts, S., Moscardini, L., Vanzella, E., et al., 2002. Measuring the redshift evolution of clustering: the Hubble Deep Field South. MNRAS 329, 355–366. doi:10.1046/j.1365-8711.2002.04988.x, arXiv:astro-ph/0109453.

Banerji, M., Jouvel, S., Lin, H., et al., 2015. Combining Dark Energy Survey Science Verification data with near-infrared data from the ESO VISTA Hemisphere Survey. MNRAS 446, 2523–2539. doi:10.1093/mnras/stu2261, arXiv:1407.3801.

Bazin, G., Ruhlmann-Kleider, V., Palanque-Delabrouille, N., et al., 2011. Photometric selection of Type Ia supernovae in the Supernova Legacy Survey. A&A 534, A43. doi:10.1051/0004-6361/201116898, arXiv:1109.0948.

Bertin, E., 2011. Automated Morphometry with SExtractor and PSFEx, in: Evans, I.N., Accomazzi, A., Mink, D.J., Rots, A.H. (Eds.), Astronomical Data Analysis Software and Systems XX, p. 435.

Bertin, E., Arnouts, S., 1996. SExtractor: Software for source extraction. A&AS 117, 393–404. doi:10.1051/aas:1996164.

Bonnett, C., Troxel, M.A., Hartley, W., others, Dark Energy Survey Collaboration, 2016. Redshift distributions of galaxies in the Dark Energy Survey Science Verification shear catalogue and implications for weak lensing. Phys. Rev. D 94, 042005. doi:10.1103/PhysRevD.94.042005, arXiv:1507.05909.

Bradley, E., Tibshirani, J., 1993. An Introduction to the Bootstrap .

Budavári, T., Szalay, A.S., Csabai, I., Connolly, A.J., Tsvetanov, Z., 2001. An Optimal Multihump Filter for Photometric Redshifts. AJ 121, 3266–3269. doi:10.1086/321068, arXiv:astro-ph/0106073.

Carlstrom, J.E., Ade, P.A.R., Aird, K.A., et al., 2011. The 10 Meter South Pole Telescope. PASP 123, 568–581. doi:10.1086/659879, arXiv:0907.4445.

Carrasco Kind, M., Brunner, R., 2014. MLZ: Machine Learning for photo-Z. Astrophysics Source Code Library. arXiv:1403.003.

Carrasco Kind, M., Brunner, R.J., 2013. TPZ: photometric redshift PDFs and ancillary information by using prediction trees and random forests. MNRAS 432, 1483–1501. doi:10.1093/mnras/stt574, arXiv:1303.7269.

Chang, C., Busha, M.T., Wechsler, R.H., et al., 2015. Modeling the Transfer Function for the Dark Energy Survey. ApJ 801, 73. doi:10.1088/0004-637X/801/2/73, arXiv:1411.0032.

Colless, M., Dalton, G., Maddox, S., et al., 2001. The 2dF Galaxy Redshift Survey: spectra and redshifts. MNRAS 328, 1039–1063. doi:10.1046/j.1365-8711.2001.04902.x, arXiv:astro-ph/0106498.

Collister, A.A., Lahav, O., 2004. ANNz: Estimating Photometric Redshifts Using Artificial Neural Networks. PASP 116, 345–351. doi:10.1086/383254, arXiv:astro-ph/0311058.

Comparat, J., Delubac, T., Jouvel, S., et al., 2016. SDSS-IV eBOSS emission-line galaxy pilot survey. A&A 592, A121. doi:10.1051/0004-6361/201527377, arXiv:1509.05045.

Cunha, C.E., Huterer, D., Lin, H., et al., 2014. Spectroscopic failures in photometric redshift calibration: cosmological biases and survey requirements. MNRAS 444, 129–146. doi:10.1093/mnras/stu1424, arXiv:1207.3347.

Cunha, C.E., Lima, M., Oyaizu, H., et al., 2009. Estimating the redshift distribution of photometric galaxy samples - II. Applications and tests of a new method. MNRAS 396, 2379–2398. doi:10.1111/j.1365-2966.2009.14908.x, arXiv:0810.2991.

Davis, M., Faber, S.M., Newman, J., et al., 2003. Science Objectives and Early Results of the DEEP2 Redshift Survey, in: Guhathakurta, P. (Ed.), Discoveries and Research Prospects from 6- to 10-Meter-Class Telescopes II, pp. 161–172. doi:10.1117/12.457897, arXiv:astro-ph/0209419.

Davis, M., Guhathakurta, P., Konidaris, N.P., et al., 2007. The All-Wavelength Extended Groth Strip International Survey (AEGIS) Data Sets. ApJ 660, L1–L6. doi:10.1086/517931, arXiv:astro-ph/0607355.

De Vicente, J., Sánchez, E., Sevilla-Noarbe, I., 2016. DNF - Galaxy photometric redshift by Directional Neighbourhood Fitting. MNRAS 459, 3078–3088. doi:10.1093/mnras/stw857, arXiv:1511.07623.

DES, et al., 2016. The Dark Energy Survey: more than dark energy - an overview. MNRAS doi:10.1093/mnras/stw641, arXiv:1601.00329.

Desai, S., Armstrong, R., Mohr, J.J., et al., 2012. The Blanco Cosmology Survey: Data Acquisition, Processing, Calibration, Quality Diagnostics, and Data Release. ApJ 757, 83. doi:10.1088/0004-637X/757/1/83, arXiv:1204.1210.

Diehl, H.T., Abbott, T.M.C., Annis, J., et al., 2014. The Dark Energy Survey and operations: Year 1, in: Observatory Operations: Strategies, Processes, and Systems V, p. 91490V. doi:10.1117/12.2056982.

Driver, S.P., Hill, D.T., Kelvin, L.S., et al., 2011. Galaxy and Mass Assembly (GAMA): survey diagnostics and core data release. MNRAS 413, 971–995. doi:10.1111/j.1365-2966.2010.18188.x, arXiv:1009.0614.

Flaugher, B., 2005. The Dark Energy Survey. International Journal of Modern Physics A 20, 3121–3123. doi:10.1142/S0217751X05025917.

Flaugher, B., Diehl, H.T., Honscheid, K., et al., 2015. The Dark Energy Camera. AJ 150, 150. doi:10.1088/0004-6256/150/5/150, arXiv:1504.02900.

Garilli, B., Guzzo, L., Scodeggio, M., et al., 2014. The VIMOS Public Extragalactic Survey (VIPERS). First Data Release of 57 204 spectroscopic measurements. A&A 562, A23. doi:10.1051/0004-6361/201322790, arXiv:1310.1008.

Garilli, B., Le Fèvre, O., Guzzo, L., et al., 2008. The Vimos VLT deep survey. Global properties of 20,000 galaxies in the $I_{AB} < 22.5$ WIDE survey. A&A 486, 683–695. doi:10.1051/0004-6361:20078878, arXiv:0804.4568.

Georgakakis, A., Mountrichas, G., Salvato, M., et al., 2014. Large-scale clustering measurements with photometric redshifts: comparing the dark matter haloes of X-ray AGN, star-forming and passive galaxies at $z \sim 1$. MNRAS 443, 3327–3340. doi:10.1093/mnras/stu1326, arXiv:1407.1863.

Gerdes, D.W., Sypniewski, A.J., McKay, T.A., et al., 2010. ArborZ: Photometric Redshifts Using Boosted Decision Trees. ApJ 715, 823–832. doi:10.1088/0004-637X/715/2/823, arXiv:0908.4085.

Giannantonio, T., Fosalba, P., Cawthon, R., et al., 2016. CMB lensing tomography with the DES Science Verification galaxies. MNRAS 456, 3213–3244. doi:10.1093/mnras/stv2678, arXiv:1507.05551.

Graff, P., Feroz, F., Hobson, M.P., et al., 2014. SKYNET: an efficient and robust neural network training tool for machine learning in astronomy. MNRAS 441, 1741–1759. doi:10.1093/mnras/stu642, arXiv:1309.0790.

Hearin, A.P., Zentner, A.R., Ma, Z., et al., 2010. A General Study of the Influence of Catastrophic Photometric Redshift Errors on Cosmology with Cosmic Shear Tomography. ApJ 720, 1351–1369. doi:10.1088/0004-637X/720/2/1351, arXiv:1002.3383.

High, F.W., Stubbs, C.W., Rest, A., et al., 2009. Stellar Locus Regression: Accurate Color Calibration and the Real-Time Determination of Galaxy Cluster Photometric Redshifts. AJ 138, 110–129. doi:10.1088/0004-6256/138/1/110, arXiv:0903.5302.

Hildebrandt, H., Arnouts, S., Capak, P., et al., 2010. PHAT: PHoto-z Accuracy Testing. A&A 523, A31. doi:10.1051/0004-6361/201014885, arXiv:1008.0658.

Honscheid, K., Elliott, A., Bonati, M., et al., 2014. The DECam DAQ System: lessons learned after one year of operations, in: Software and Cyberinfrastructure for Astronomy III, p. 91520G. doi:10.1117/12.2057073.

Hoyle, B., Rau, M.M., Bonnett, C., et al., 2015. Data augmentation for machine learning redshifts applied to Sloan Digital Sky Survey galaxies. MNRAS 450, 305–316. doi:10.1093/mnras/stv599, arXiv:1501.06759.

Huterer, D., Kim, A., Krauss, L.M., et al., 2004. Redshift Accuracy Requirements for Future Supernova and Number Count Surveys. ApJ 615, 595–602. doi:10.1086/424726, arXiv:astro-ph/0402002.

Ilbert, O., Arnouts, S., McCracken, H.J., et al., 2006. Accurate photometric redshifts for the CFHT legacy survey calibrated using the VIMOS VLT deep survey. A&A 457, 841–856. doi:10.1051/0004-6361:20065138, arXiv:astro-ph/0603217.

Jiang, L., Fan, X., Bian, F., McGreer, et al., 2014. The Sloan Digital Sky Survey Stripe 82 Imaging Data: Depth-optimized Co-adds over 300 deg^2 in Five Filters. ApJS 213, 12. doi:10.1088/0067-0049/213/1/12, arXiv:1405.7382.

Jones, D.H., Read, M.A., Saunders, W., et al., 2009. The 6dF Galaxy Survey: final redshift release (DR3) and southern large-scale structures. MNRAS 399, 683–698. doi:10.1111/j.1365-2966.2009.15338.x, arXiv:0903.5451.

Kaiser, N., Burgett, W., Chambers, K., et al., 2010. The Pan-STARRS wide-field optical/NIR imaging survey, in: Society of Photo-Optical Instrumentation Engineers (SPIE) Conference Series, p. 0. doi:10.1117/12.859188.

Kessler, R., Marriner, J., Childress, M., et al., 2015. The Difference Imaging Pipeline for the Transient Search in the Dark Energy Survey. AJ 150, 172. doi:10.1088/0004-6256/150/6/172, arXiv:1507.05137.

Koposov, S., Bartunov, O., 2006. Q3C, Quad Tree Cube – The new Sky-indexing Concept for Huge Astronomical Catalogues and its Realization for Main Astronomical Queries (Cone Search and Xmatch) in Open Source Database PostgreSQL, in: Gabriel, C., Arviset, C., Ponz, D., Enrique, S. (Eds.), Astronomical Data Analysis Software and Systems XV, p. 735.

Le Fèvre, O., Vettolani, G., Garilli, B., et al., 2005. The VIMOS VLT deep survey. First epoch VVDS-deep survey: 11 564 spectra with $17.5 \leq IAB \leq 24$, and the redshift distribution over $0 \leq z \leq 5$. A&A 439, 845–862. doi:10.1051/0004-6361:20041960, arXiv:astro-ph/0409133.

Le Fèvre, O., Vettolani, G., Paltani, S., et al., 2004. The VIMOS VLT Deep Survey. Public release of 1599 redshifts to $I_{AB} \leq 24$ across the Chandra Deep Field South. A&A 428, 1043–1049. doi:10.1051/0004-6361:20048072, arXiv:astro-ph/0403628.

Lidman, C., Ardila, F., Owers, M., et al., 2016. The XXL Survey XIV. AAOmega Redshifts for the Southern XXL Field. PASA 33, e001. doi:10.1017/pasa.2015.52, arXiv:1512.04662.

Lidman, C., Ruhlmann-Kleider, V., Sullivan, M., et al., 2013. An Efficient Approach to Obtaining Large Numbers of Distant Supernova Host Galaxy Redshifts. PASA 30, e001. doi:10.1017/pasa.2012.001, arXiv:1205.1306.

Lilly, S.J., Le Brun, V., Maier, C., et al., 2009. The zCOSMOS 10k-Bright Spectroscopic Sample. ApJS 184, 218–229. doi:10.1088/0067-0049/184/2/218.

Lima, M., Hu, W., 2007. Photometric redshift requirements for self-calibration of cluster dark energy studies. Phys. Rev. D 76, 123013. doi:10.1103/PhysRevD.76.123013, arXiv:0709.2871.

Ma, Z., Bernstein, G., 2008. Size of Spectroscopic Calibration Samples for Cosmic Shear Photometric Redshifts. ApJ 682, 39–48. doi:10.1086/588214, arXiv:0712.1562.

Ma, Z., Hu, W., Huterer, D., 2006. Effects of Photometric Redshift Uncertainties on Weak-Lensing Tomography. ApJ 636, 21–29. doi:10.1086/497068, arXiv:astro-ph/0506614.

Mao, M.Y., Sharp, R., Norris, R.P., et al., 2012. The Australia Telescope Large Area Survey: spectroscopic catalogue and radio luminosity functions. MNRAS 426, 3334–3348. doi:10.1111/j.1365-2966.2012.21913.x, arXiv:1208.2722.

Melchior, P., Sheldon, E., Drlica-Wagner, A., et al., 2016. Crowdsourcing quality control for Dark Energy Survey images. Astronomy and Computing 16, 99–108. doi:10.1016/j.ascom.2016.04.003, arXiv:1511.03391.

Mohr, J.J., Armstrong, R., Bertin, E., et al., 2012. The Dark Energy Survey data

processing and calibration system, in: Society of Photo-Optical Instrumentation Engineers (SPIE) Conference Series, p. 0. doi:10.1117/12.926785, arXiv:1207.3189.

Moles, M., Benítez, N., Aguerri, J.A.L., et al., 2008. The Alhambra Survey: a Large Area Multimedium-Band Optical and Near-Infrared Photometric Survey. AJ 136, 1325–1339. doi:10.1088/0004-6256/136/3/1325, arXiv:0806.3021.

Momcheva, I.G., Brammer, G.B., van Dokkum, P.G., et al., 2016. The 3D-HST Survey: Hubble Space Telescope WFC3/G141 Grism Spectra, Redshifts, and Emission Line Measurements for ˜ 100,000 Galaxies. ApJS 225, 27. doi:10.3847/0067-0049/225/2/27, arXiv:1510.02106.

Muzzin, A., Wilson, G., Yee, H.K.C., et al., 2012. The Gemini Cluster Astrophysics Spectroscopic Survey (GCLASS): The Role of Environment and Self-regulation in Galaxy Evolution at z ˜ 1. ApJ 746, 188. doi:10.1088/0004-637X/746/2/188, arXiv:1112.3655.

Newman, J.A., 2008. Calibrating Redshift Distributions beyond Spectroscopic Limits with Cross-Correlations. ApJ 684, 88–101. doi:10.1086/589982, arXiv:0805.1409.

Parkinson, D., Riemer-Sørensen, S., Blake, C., et al., 2012. The WiggleZ Dark Energy Survey: Final data release and cosmological results. Phys. Rev. D 86, 103518. doi:10.1103/PhysRevD.86.103518, arXiv:1210.2130.

Prévot, M.L., Lequeux, J., Prévot, L., et al., 1984. The typical interstellar extinction in the Small Magellanic Cloud. A&A 132, 389–392.

Rest, A., Scolnic, D., Foley, R.J., et al., 2014. Cosmological Constraints from Measurements of Type Ia Supernovae Discovered during the First 1.5 yr of the Pan-STARRS1 Survey. ApJ 795, 44. doi:10.1088/0004-637X/795/1/44, arXiv:1310.3828.

Sadeh, I., Abdalla, F.B., Lahav, O., 2016. ANNz2: Photometric Redshift and Probability Distribution Function Estimation using Machine Learning. PASP 128, 104502. doi:10.1088/1538-3873/128/968/104502, arXiv:1507.00490.

Sánchez, C., Carrasco Kind, M., Lin, H., et al., 2014. Photometric redshift analysis in the Dark Energy Survey Science Verification data. MNRAS 445, 1482–1506. doi:10.1093/mnras/stu1836, arXiv:1406.4407.

Schlegel, D.J., Finkbeiner, D.P., Davis, M., 1998. Maps of Dust Infrared Emission for Use in Estimation of Reddening and Cosmic Microwave Background Radiation Foregrounds. ApJ 500, 525–553. doi:10.1086/305772, arXiv:astro-ph/9710327.

Scolnic, D., Rest, A., Riess, A., et al., 2014. Systematic Uncertainties Associated with the Cosmological Analysis of the First Pan-STARRS1 Type Ia Supernova Sample. ApJ 795, 45. doi:10.1088/0004-637X/795/1/45, arXiv:1310.3824.

Scoville, N., Abraham, R.G., Aussel, H., et al., 2007. COSMOS: Hubble Space Telescope Observations. ApJS 172, 38–45. doi:10.1086/516580, arXiv:astro-ph/0612306.

Shectman, S.A., Landy, S.D., Oemler, A., et al., 1996. The Las Campanas Redshift Survey. ApJ 470, 172. doi:10.1086/177858, arXiv:astro-ph/9604167.

Silverman, J.D., Kashino, D., Sanders, D., Kartaltepe, J.S., et al., 2015. The FMOS-COSMOS Survey of Star-forming Galaxies at z˜1.6. III. Survey Design, Performance, and Sample Characteristics. ApJS 220, 12. doi:10.1088/0067-0049/220/1/12, arXiv:1409.0447.

Stalin, C.S., Petitjean, P., Srianand, R., et al., 2010. Optical identification of XMM sources in the Canada-France-Hawaii Telescope Legacy Survey. MNRAS 401, 294–306. doi:10.1111/j.1365-2966.2009.15636.x, arXiv:0909.0464.

Sullivan, M., Conley, A., Howell, D.A., et al., 2011. VizieR Online Data Catalog: Type Ia supernovae luminosities (Sullivan+, 2010). VizieR Online Data Catalog 740.

Tasca, L.A.M., Le Fevre, O., Ribeiro, B., et al., 2016. The VIMOS Ultra Deep Survey First Data Release: spectra and spectroscopic redshifts of 698 objects up to z˜6 in CANDELS. ArXiv e-prints arXiv:1602.01842.

Treu, T., Schmidt, K.B., Brammer, G.B., et al., 2015. The Grism Lens-Amplified Survey from Space (GLASS). I. Survey Overview and First Data Release. ApJ 812, 114. doi:10.1088/0004-637X/812/2/114, arXiv:1509.00475.

Yuan, F., Lidman, C., Davis, T.M., et al., 2015. OzDES multifibre spectroscopy for the Dark Energy Survey: first-year operation and results. MNRAS 452, 3047–3063. doi:10.1093/mnras/stv1507, arXiv:1504.03039.